Research article

Synergy between MgO and TiO$_2$ doped with Mn^{2+} ions for supercapacitor applications

Mohamad Hasan Aleinawi[a,1], Maria Stefan[b,1], Eminenur Saritas[a], Abdalla Hroub[a], Feray Bakan-Misirlioglu[d], Sergiu Macavei[b], Lucian Barbu Tudoran[b,c], Kuray Dericiler[a,e], Burcu Saner Okan[e], Emre Erdem[a,e,*], Arpad Mihai Rostas[b,**]

[a] Faculty of Engineering and Natural Sciences, Sabanci University, Tuzla, Istanbul, 34956, Turkey
[b] National Institute for Isotopic and Molecular Technologies, Donat 67-103, Cluj-Napoca, 400293, Romania
[c] Faculty of Biology and Geology, Babes-Bolyai University, 44 Republicii, Cluj-Napoca, 400015, Romania
[d] Nanotechnology Research and Application Center (SUNUM), Sabanci University, Tuzla, Istanbul, 34956, Turkey
[e] Integrated Manufacturing Technologies Research and Application Center and Composite Technologies Center of Excellence, Sabanci University, Teknopark Istanbul, Pendik, Istanbul, 34906, Turkey

ARTICLE INFO

ABSTRACT

Supercapacitors are unique energy storage devices that bridge the gap between Li-ion batteries and conventional capacitors with higher power/energy densities, longer life cycles, and more rapid charge/discharge rates. Research efforts are concentrated on optimizing the performance of supercapacitors (SCs), addressing a crucial component of these devices: the electrode materials, which should provide large active surface areas, display high electrical conductivities, and possess stable chemical properties. To achieve this, in this study, undoped and Mn-doped MgO−TiO$_2$ nanocrystals and coffee-waste-derived carbon were used as electrode materials for symmetric and asymmetric supercapacitors yielding adequate performance. The structural study was performed by X-ray diffraction and Raman analysis, showing a phase mixture of tetragonal Anatase TiO$_2$, cubic MgO, and orthorhombic MgTi$_2$O$_5$ nanocrystals. Electron paramagnetic resonance and photoluminescence spectroscopy analysis were used to provide insight into the defective structure of the composites. The electrochemical performance was tested by cyclic voltammetry, impedance, voltage holding, and galvanostatic cycling with potential limitations. The SCs exhibited promising results for specific capacitances up to 100 and 221 F/g for symmetric and asymmetric (containing coffee-waste-derived carbon as a counter electrode) supercapacitor devices, respectively. At the same time, enhanced energy and power density values of 30.7 Wh/kg and 122.8 kW/kg were reached.

1. Introduction

In the past 2 decades, worldwide electricity consumption has nearly doubled, as stated by the International Energy Agency [1]. Consequently, the reliance on fossil fuels, such as coal, oil, and natural gas, has persisted to our current days, drastically increasing greenhouse gas emissions in the atmosphere. Due to the shortage of fossil fuel reserves and an amplified global awareness to reduce industrial pollutants, the shift to energy production from renewable sources and the design of energy storage devices to collect and store excess energy from intermittent sources has become of utmost importance [2]. In recent years,

researchers extensively explored supercapacitors (SCs) as unique energy storage devices that bridge the gap between Li-ion batteries and conventional capacitors with higher power/energy densities, longer life cycles, and more rapid charge/discharge rates [3], seeking to satisfy public demand for portable electronic devices, electric vehicles, and industrial equipment, research efforts are concentrated on optimizing the performance of SCs, addressing a crucial component of these devices: the electrode materials [4,5]. Electrode materials should provide large active surface areas, display high electrical conductivities, and possess stable chemical properties at a cost-effective price [6]. SCs can be categorized based on their charge storage mechanisms and the

---

electrode materials employed during the device's design. Electric double-layer capacitors (EDLCs) store charge through the reversible adsorption of ions. The electrode materials used in EDLC-type SCs are carbon-based active materials with high surface areas. Pseudo-capacitors (redox SCs) utilize fast and reversible reduction-oxidation reactions (or faradaic reactions) at the electrode-electrolyte interface. Typical materials used in pseudo-capacitors include transition metals and conducting polymers [7,8]. Asymmetric SCs, also called hybrid SCs, store charge through a combination of EDLC and pseudo-capacitor mechanisms. In asymmetric SCs, one electrode stores charge electrostatically while the other electrode undergoes faradaic reactions, contributing to additional energy storage. Metal oxides (MOs) act as ideal electrode materials and have proven to exhibit all the properties above, amplifying the specific capacitance significantly [9,10]. Hybrid MOs assemble the best of both MO features and potentially optimize the efficiency of SC devices.

Magnesium Oxide (MgO) in the form of nanoparticles has a spinel morphology, exhibiting average diameters between 5 and 100 nm and specific surface areas ranging from 25 to 50 m^2/g [11]. MgO has been researched as an electrode material, proving to be an ideal candidate due to its good chemical stability, high melting points, strong acid/base corrosion resistance, potential conductivity in the presence of extrinsic defects (through doping), high dielectric constant value, and redox-activity in Faradic reactions [12]. MgO's high specific capacitance (C_P) reflects its large electrical energy storage capacity per unit mass or volume. Its high electrical and thermal conductivity facilitates faster ion movement through electrode materials with certain morphologies, resulting in rapid charging and discharging mechanisms. It also improves overall performance by reducing energy losses caused by internal resistance [13].

Gaikwad et al. [14] reported promising results regarding MgO nanospheres that exhibited an C_P of 536.06 F/g. The study revealed values of specific energy and specific power that reached as high as 30.79 Wh/kg and 1420 W/kg, respectively, at 2 mA/cm^2 in 1 M KOH. The electrochemical impedance spectroscopy (EIS) plots showed good power performance and cycling capability, retaining 91.38% capacitance after 5000 CV cycles. The C_P of the MgO//AC asymmetric device yielded 210.21 F/g at 5 mV/s in a PVA-KOH solid-state electrolyte. The performance of the asymmetric supercapacitor demonstrated that the MgO-based electrode is appropriate for use in real device manufacture, with an energy density of 23.90 Wh/kg and a power density of 1.84 kW/kg. This study proves the usefulness of the simple and cost-effective successive ionic layer adsorption and reaction (SILAR) method for synthesizing pure MgO nanostructures as electrodes in supercapacitors. Another successful study utilizing the SILAR technique was reported by Suryawanshi et al. [15]. BaO thin films were used as electrodes in SC devices, revealing an excellent cycling capability that retains 91.1% capacitance retention after 7500 cycles. The C_P was 405.72 F/g at a 5 mV/s scan rate in 1 M KOH electrolyte. The maximum energy and power density values obtained were 53.57 Wh/kg and 2390 W/kg, respectively.

Several studies on Transition Metal (TM)-doped MgO have reported that extrinsically defected MgO displays improved catalytic and electrochemical properties [16–18]. Mn-doping was associated with modified electrode materials and improved overall electrochemical performance [19,20]. Kuraganti et al. [21] proved an optimized charge-transfer mechanism upon doping MoSe$_2$ nanoflowers with Mn that contributed to forming Se vacancies. Yuan et al. [22] demonstrated increased specific capacitances upon doping NiMoO$_4$ nanorods with Mn that formed convenient defects that resulted in enhanced electron migration. Furthermore, Zhang et al. [23] reported enhanced capacities and better cyclic stabilities of Ni(OH)$_2$ electrode SCs upon doping with Mn. Firstly, Mn ions decreased the energy required for surface dehydrogenation, thus ultimately increasing the conductivity of the electrode material [24]. Secondly, the high valency of Mn ions intensified the electrostatic attraction between the nanosheet cations and the

hydroxyl interlayer anions. This led to a larger exposure of electrochemically active sites and, subsequently, faster Faradic redox reactions [25]. Overall, many researchers have concluded the prominence of Mn-doping concerning the generation of defective sites, the expansion of interlayer morphologies, and the facilitation of a more rapid and efficient electron transfer [24].

On the other hand, Titanium Dioxide (TiO$_2$) is another prominent semiconductor material with attractive properties: cheap, abundant, environmentally friendly, and non-toxic [26]. TiO$_2$ has become a hot spot for researchers in multidisciplinary applications of energy storage systems, especially as electrode material in SCs [27]. This is due to this semiconductor being physically/chemically stable and providing high energy densities with good cyclic stabilities/efficiencies [28]. He et al. [29] synthesized Mn-doped TiO$_2$ nanotube cathodes, producing asymmetric SCs that retained approximately 92% of capacitance after 5000 cycles, with a prominent value of volumetric capacitance reaching up to 1051 F/cm^3. Furthermore, many studies explored the utilization of binary and ternary TiO$_2$-based composites as electrodes in asymmetric SCs with carbon nanotubes as the other electrodes. Such SCs demonstrated specific capacitance values that reached as high as 346 F/g at a current density of 1 A/g and 580 F/g at a current density of 2.6 A/g, with impressive rate capabilities and cyclabilities [29–31]. Utilizing TiO$_2$ as electrode material in various SC devices yields poor capacitance results, as reported in the literature, which is attributed to the fact that the intrinsic phases of TiO$_2$ combined with the wide energy gap of the material restrict the electrical conductivity [32].

Nonetheless, doping TiO$_2$ with TMs modifies the optoelectronic properties of the material, whereas Manganese (Mn) - doped TiO$_2$ displayed incredible capacitive performance, excellent charge/discharge rate, and superior cycling performance [33]. Mn as a TM dopant in MO electrodes such as MgO and TiO$_2$ has been reported as the best 3d-TM dopant due to the production of intermediate donor states inside the forbidden gaps with fewer defective sites and the enhancement of charge mobility. Ojha et al. [33] investigated mesoporous Mn-doped TiO$_2$ nanoparticles synthesized via the sol-gel route. They found that Mn doping has increased the surface area, improved the mesoporosity, and created more active sites, ultimately leading to incredible capacitive performance.

The role of Mn doping in enhancing electrochemical properties has been studied extensively in materials like ZnO, WO$_3$ and KNN, and it is a key focus of our research [34–37]. Mn doping changes the electronic structure of the host materials, which influences their functional properties. A critical factor is the solubility of Mn ions in the host lattice. When Mn ions are properly incorporated into the crystal lattice, distinct Electron Paramagnetic Resonance (EPR) signals appear, revealing valuable insights into the local electronic environment [38]. However, excessive Mn doping can lead to negative effects, such as dipolar broadening of the EPR signals and grain boundary issues, which obscure hyperfine features and indicate Mn clustering or segregation instead of uniform substitution. These issues can create structural and electronic inhomogeneities, lowering the material's performance. In MgO and TiO$_2$, Mn doping provides specific advantages over other dopants by modifying the band structure and enhancing charge transport. In MgO, Mn ions can act as electron traps or aid defect engineering, improving charge storage and electrochemical activity, while in TiO$_2$, Mn reduces recombination rates by introducing intermediate states in the band gap, enhancing photocatalytic and energy storage applications. Testing solubility limits and the local electronic structure using EPR helps control Mn's distribution and oxidation states, directly influencing electrochemical performance, understanding that allows fine-tuning the material properties and developing a controlled doping strategy that highlights Mn's unique advantages while minimizing adverse effects, setting it apart from other dopants.

Recently, to address the limitations of TMOs as electrodes while simultaneously exploiting their intrinsic features in electrochemical applications without compromising their inherent pseudocapacitance,

researchers have been intrigued to investigate potential synergetic effects among different MOs to achieve composite MO-based Hybrid SCs (HSC) [39]. Such hybrid MO-based SCs have been proven to achieve enhanced electrical conductivities and ion intercalations [40]. Toward this end, in this work, undoped and Mn-doped TiO_2 nanoparticles are grown on undoped and Mn-doped MgO nanosheets to create an onion-like MO composite structure to be used as an electrode material for symmetric SC applications. Highlighting the cruciality of sustainable engineering and complying with the need to reduce pollutant and greenhouse gas emissions, eco-friendly methods to construct the counter electrode in asymmetric SC devices are explored. The coffee industry reportedly produces approximately 8 million tonnes of environmentally dangerous pollutants yearly, such as tannins, polyphenols, and caffeine [41]. Recycling/upcycling waste and biomass, such as coffee, into useful materials is one sustainable solution for safely disposing of toxic pollutants [42]. Recently, there have been many studies involving natural, eco-friendly, renewable, and inexpensive precursor biomass materials to produce activated carbon, such as bamboo [43], dragon fruit [44], walnuts [45], and prawns [46]. Herein, we report using coffee waste as a precursor biomass material to produce the C-based (coffee-carbon CC) counter electrodes in our composite MO/CC SCs.

2. Experimental

2.1. Materials and synthesis

The materials and solvents used to prepare the $MgO-TiO_2$ nanocomposites were $MgNO_3 \cdot 6H_2O$ magnesium nitrate hexahydrate (for synthesis, Merck) as a magnesium source, $Ti(^iOC_3H_7)_4$ – TIPO tetraisopropyl ortotitanate (for synthesis, Merck) as a titanium source, $Mn(NO_3)_2 \cdot 6H_2O$ manganese nitrate tetrahydrate (for analysis, Merck) as Mn dopant (0.5, 1 mol%), NaOH sodium hydroxide (Merck) as precipitating agent, C_2H_5OH - EtOH ethanol (absolute for synthesis, Merck), CH_3COOH - AcOH acetic acid glacial (p.a., Merck), $CH_3COCH_2COCH_3$ - acac acetylacetone (p.a., Alfa Aesar). All chemicals have analytical grade without further purification and were used as received (Scheme 1).

The $MgO-TiO_2$ nanocomposites were obtained (see Scheme 2) by combining the synthesis of MgO nanoparticles with the chemical precipitation method and TiO_2 with the sol-gel process. Thus, 1 g of $MgNO_3 \cdot 6H_2O$ and 2 different $Mn(NO_3)_2 \cdot 6H_2O$ concentrations (0.5 mol% and 1 mol%) were dissolved in 50 mL of distilled water under magnetic stirring to synthesize the MgO nanoparticles. Subsequently, a 2 M NaOH solution was added to the above solution to maintain the pH value at
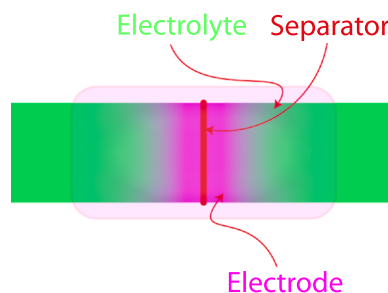
**Scheme 2.** Schematic representation of the SC device components used in this study. SC = supercapacitor.

around 12. The white precipitate obtained was continuously stirred for 4 h at room temperature. After washing and separating, the obtained powder was annealed at 400 °C for 2 h. The same procedure, with minor modifications, was reported in a previous study by Hroub et al. [12].

To synthesize the $MgO-TiO_2$ nanocomposites, 2 mM of MgO nanoparticles were sonicated in 50 mL of ethanol under an argon environment. Following that, 4 mL of TIPO, 2 different $Mn(NO_3)_2 \cdot 6H_2O$ concentrations (0.5 mol% and 1 mol%), and 0.5 mL of AcOH were added. The pH value was set at 3. The stirring was continued for 2 h before adding 2 mL acac. TIPO and acac had a molar ratio of 2:1. TiO_2 is generated via hydrolysis and condensation of TIPO in the presence of MgO nanoparticles, forming $MgO-TiO_2$ nanocomposites. The obtained sol samples were exposed to air for an extended period until the solvents were gradually removed, which led to the formation of a gel. The resulting products were dried in an oven at 65 °C before being thermally treated for 2 h at 550 °C to form crystallized $MgO-TiO_2$ nanocomposites. Previous studies have reported the procedure for generating nanocomposites in 2 synthesis phases, with improvements for experimental settings suitable for $MgO-TiO_2$ synthesis [47].

For this study, 5 $MgO-TiO_2$-based (undoped or Mn-doped) samples were prepared: $MgO-TiO_2$, MgO:Mn0.5-TiO_2, MgO:Mn1-TiO_2, $MgO-TiO_2$:Mn0.5, and $MgO-TiO_2$:Mn1, where 0.5 and 1 show the Mn-ions molar doping concentration (%). In the composite samples, the doping process was carried out by combining one doped component with another undoped one.

2.2. Morpho-structural characterizations

X-ray diffraction (XRD) measurements were performed on a Smart Lab Rigaku diffractometer with Cu-Kα radiation (λ = 1.54 Å). All
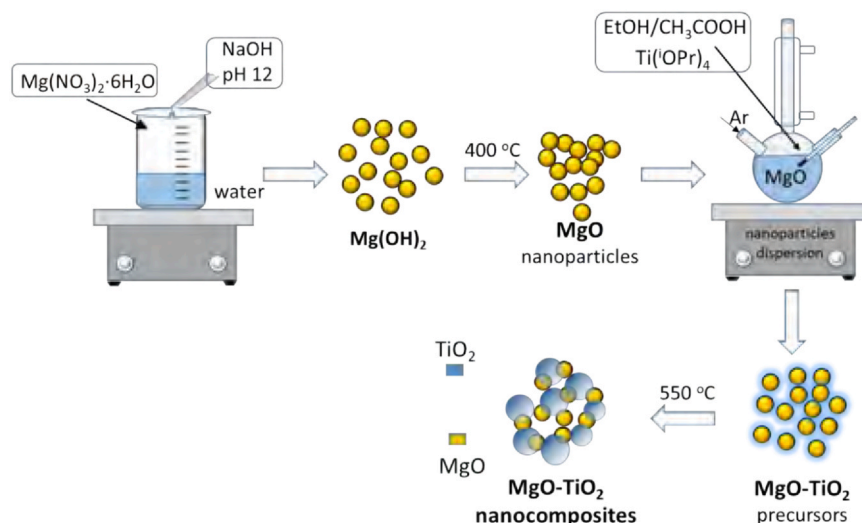
Scheme 1. Schematic illustration of the synthesis process of undoped and Mn-doped $MgO-TiO_2$ nanocomposites.

measurements were carried out at room temperature in a 10–90° range, with a 0.01° step.

In addition to the XRD analysis, we conducted Raman spectroscopy to investigate the potential phononic mode changes within the MgO and TiO_2 structures resulting from Mn site doping. The Raman scattering was recorded using an InVia Raman Spectrometer (Renishaw, UK) with an upright microscope and a 532 nm frequency-doubled Nd:YAG-solid phase laser. 1% laser power is used to prevent the degradation of samples by the laser during data acquisition.

The morphology of the $MgO-TiO_2$ samples was evidenced using scanning transmission electron microscopy (STEM), which was carried out on a Hitachi HD-2700 microscope at a 200 kV electron acceleration, coupled with a double energy dispersive spectroscopy (EDS) detector (Oxford Instruments, Oxford, UK, AZtec Software, version 3.3). A 300-mesh copper electrolytic grid was used as a sample holder, to which a carbon film was attached.

An FS5 Spectrofluorometer from Edinburgh Instruments was employed for the photoluminescence (PL) analysis. The measurements were carried out at room temperature with a 300 nm (3.54 eV) excitation wavelength.

Electron paramagnetic resonance spectroscopy was performed on a continuous wave dual band X and Q-band spectrometer Bruker ELEXSYS E500. An ER 5106 QT standard Bruker cavity operating at 34 GHz was employed for the Q-Band measurements.

2.3. Electrochemical measurements

Electrochemical (EC) measurements were performed using a Biologic VMP 300 multipotentiostat with the standard 2-electrode technique. The electrolyte used for all the test samples was a 6 M KOH solution with glass fiber as a separator in a symmetric configuration. The concentration of the KOH electrolyte was selected based on several previous studies suggesting the superiority of 6 M over lower and higher concentrations, providing enough ionic charges for the double layer, accompanied by high ionic conductivity [48]. A schematic representation of the SC design is provided in Scheme 2. In the asymmetric design, coffee-waste-derived carbon was used as a counter electrode. The synthesis procedure for obtaining this material and thorough characterization of it is presented by Dericiler et al. [49]. Briefly, waste coffee obtained from different filter coffee machines was dried and pyrolyzed in a rotary furnace under a protective Ar atmosphere at 1000 °C for 5 s. Furthermore, structural, morphological, and chemical characteristics of CC were also performed and reported in detail, showing that the flash pyrolysis process led to the formation of graphene-like structures. The transformation of coffee waste into carbonaceous structures through carbonization is often realized in batches over several hours [50] and requires pre- or post-treatments such as chemical activation [51] or ball milling [52]. However, the process utilized in this study [49] proposes semi-continuous carbonization without any chemical activation, particle size homogenization, or long process duration, where the process is only interrupted for feeding the precursor. Therefore, although this study is limited by lab-scale production with a yield of around 15%, scaling up with a large enough feedstock, a flow-controlled feeder system, and periodic product collection should be highly possible.

Carbon from coffee waste has several functional and environmental benefits over sustainable carbon sources like biochar, plant biomass, and algae. Environmentally, it offers the advantages of waste utilization, a reduced carbon footprint, and efficient energy utilization. Functionally, coffee waste-derived carbon exhibits good electrical conductivity. It can also be modified to possess a high surface area and porosity - properties critical to the SC's performance. Although the mechanical strength of coffee waste carbon is lower than traditional AC electrodes, the negligible cost of recycling the waste in supercapacitor applications remains a dominant factor. Thus, coffee-waste-derived carbon is a promising material for environmentally conscious energy

storage and sensor technologies, offering a balance of functional performance and sustainability. Gómez Urbano et al. [53] reported graphene-coffee waste-derived carbon composites as electrodes for optimized lithium-ion capacitors (LIC). Assembled LICs displayed promising values, retaining above 80% of the initial capacitance after 3000 cycles.

The electrochemical performance of the electrode material was tested using Cyclic Voltammetry (CV), Galvanostatic cycling with Potential Limitation technique (GCPL), and Potentiostatic Electrochemical Impedance Spectroscopy (PEIS). CV curves were recorded in a voltage range of 0 to +1 V at scan rates ranging from 10 to 200 mV/s. PEIS results were completed by applying a sinusoidal signal of 10 mV in a 10–1 MHz frequency range. GCPL was done in a voltage window from −1 to +1 V at a specific current of 0.1 A/g. Furthermore, the Dunn method was applied to distinguish between the capacitive and diffusive contributions in the working mechanism of the SC devices [54]. The method was conducted by applying CV tests at several convergent scan rates, then estimating the oxidation current and plotting ($i(v)/v^{1/2}$ vs $v^{1/2}$), and determining the capacitive and diffusive current values from the slope and y-intercept of the linear fit of the obtained values.

3. Results and discussion

The XRD analysis provides insight into the samples' crystal structure and lattice parameters. Rietveld refinement has been implemented to reveal the structure's phases and retrieve the lattice parameter values. Fig. 1 and Supplementary Fig. S-XRD show the results of the XRD measurement carried out on the undoped and Mn-doped $MgO-TiO_2$ samples. TiO_2 is known to crystallize in 3 main phases: Rutile, Brookite, and Anatase. The formation of the phases mentioned above is related to the stability of the crystal structure, which is determined by various factors such as synthesis method, crystallite size, pH value, and surface energy [55].

The XRD peaks of the Anatase TiO_2 phase present at 25, 38, 48, 53, 55, and 62° correspond to the (101), (112), (200), (105), (211), and (204) planes respectively. Additionally, the presence of the cubic MgO phase peaks can be noticed at 38, 43, and 63°, corresponding to the (111), (002), and (202) planes, respectively. Similar results have been reported in previous studies [56] where a MgO, TiO_2, $MgTiO_3$ and Mg_2TiO_4 phase mixture was observed. In the presented samples, no $MgTiO_3$ or Mg_2TiO_4 phases were observed. Furthermore, the formation of additional peaks that don't belong to pure TiO_2 or MgO phases is noticed around 17, 32, 41, and 42°. At first glance, these peaks seem related to the brookite phase of TiO_2. However, Raman results (see
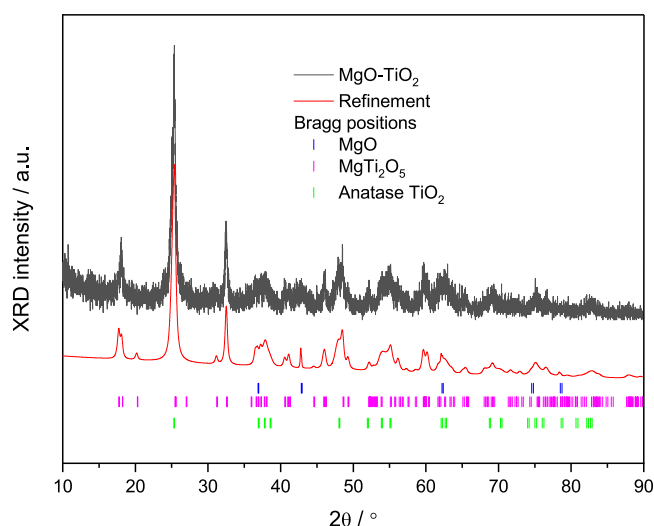

Fig. 1. Rietveld refinement of the undoped $MgO-TiO_2$.

Table 1

Cell volume (CV), the average crystallite size (ACS) and phase proportion of the main 3 phases MgO, MgTi$_2$O$_5$, and anatase TiO$_2$ determined by the Rietveld refinement

	MgO %	CV Å^3	ACS nm	MgTi$_2$O$_5$ %	CV Å^3	ACS nm	TiO$_2$ %	CV Å^3	ACS nm
MgO − TiO$_2$	10	75	200	40	364	36	50	137	21
MgO:0.5Mn-TiO$_2$	15	75	205	55	360	32	30	137	34
MgO:1Mn-TiO$_2$	15	75	205	40	365	28	45	137	25
MgO − TiO$_2$:0.5Mn	10	75	205	60	364	23	30	137	23
Mg-TiO$_2$:1Mn	10	75	205	55	360	27	35	137	137

Raman section) show no sign of the brookite phase. These peaks are most likely correlated to the formation of a Magnesium Dititanium Oxide MgTi$_2$O$_5$ phase corresponding to planes (200), (230), (240), and (420), respectively, as reported previously [57,58].

For a better understanding of the material's structure, Rietveld refinement has been applied using the Cmcm, I41amd:1, and Fm-3m spacegroups for MgTi$_2$O$_5$, Anatase TiO$_2$, and MgO, using the PDFs 2002319, 1010942, 1000053 respectively. Fig. 1 shows the Rietveld refinement for the undoped MgO − TiO$_2$ sample, while the Mn-doped MgO − TiO$_2$ refinements are presented in Supplementary Fig. S-XRD.

The refinement results confirm the presence of the Anatase TiO$_2$ phase and MgTi$_2$O$_5$ as the main phases in all samples (between 85% and 90%). The MgTi$_2$O$_5$ phase consists of an orthorhombic crystal structure, accompanied by a tetragonal structure of the Anatase TiO$_2$ phase and a cubic structure of MgO. The refinement results are summarized in Table 1 (for more details, see Supplementary Table T-Rietveld) and show the main crystallite size evolution for all 3 phases observed in the undoped and Mn-doped MgO − TiO$_2$ samples. The resemblance of the brookite phase could be related to the stability of the TiO$_2$ phase. In their study, Zhang and Banfield [59] reported that the TiO$_2$ brookite phase is the most thermodynamically stable phase for crystal sizes between 20 and 35 nm. However, the Raman results do not show any signal of brookite. A slight shift of the lattice parameters can be observed due to the Mn dopant, which confirms the successful incorporation of Mn ions into the crystal structure. Additionally, the results reveal a change in the constituents' phases. However, as the dopant percentage is small, no change in the peak positions was observed.

Fig. 2 illustrates the comparative Raman spectra of the undoped and Mn-doped MgO − TiO$_2$ samples. Titanium dioxide is naturally found in three distinct crystalline modifications: rutile (tetragonal), anatase (tetragonal), and brookite (orthorhombic). First-order Raman scattering on rutile TiO$_2$ gives rise to four Raman-active vibrational modes: A1g, B1g, B2g, and Eg. In the case of anatase TiO$_2$, 6 Raman-active vibrational modes are observed: A1g, 2B1g, and 3Eg [60]. In Fig. 2(a), the black spectrum displays distinct bands observed at approximately 146 (Eg), 197 (Eg), 400 (B1g), 520 (A1g + B1g), and 640 cm^{-1}(Eg). These observations prove the TiO$_2$ under investigation exists in the anatase phase [60]. The Raman band, centered around 146 cm^{-1}, is characterized by its high intensity and sharp profile. Interestingly, this band's frequency in anatase closely resembles that of the B1 mode in rutile (at $\approx$143 cm^{-1}), known for its sharp yet feeble appearance. In Fig. 2(b), it can be seen that doping the anatase TiO$_2$ phase with Mn ions caused a blueshift. However, the congruence between the Raman band positions of undoped and Mn-doped TiO$_2$ substantiates the presence of an anatase structural configuration within the pure and Mn-doped TiO$_2$. As for MgO, the potential Raman-active modes encompass A1g, Eg, and T2g. However, these corresponding bands could not be observed in the spectra, which can be explained as the sufficient excitation of the lattice structure of the material due to the use of very low laser energy during the analysis. In our previous work, the maximum laser power was used to excitation the MgO structures [12]. However, in this study, we could not use a higher laser power according to the relatively sensitive behavior of the samples.

Fig. 2(b) shows that doping the anatase TiO$_2$ phase with Mn ions induces a blue shift in the Raman spectrum. Such a shift typically reflects changes in the vibrational energy of molecular or lattice modes,
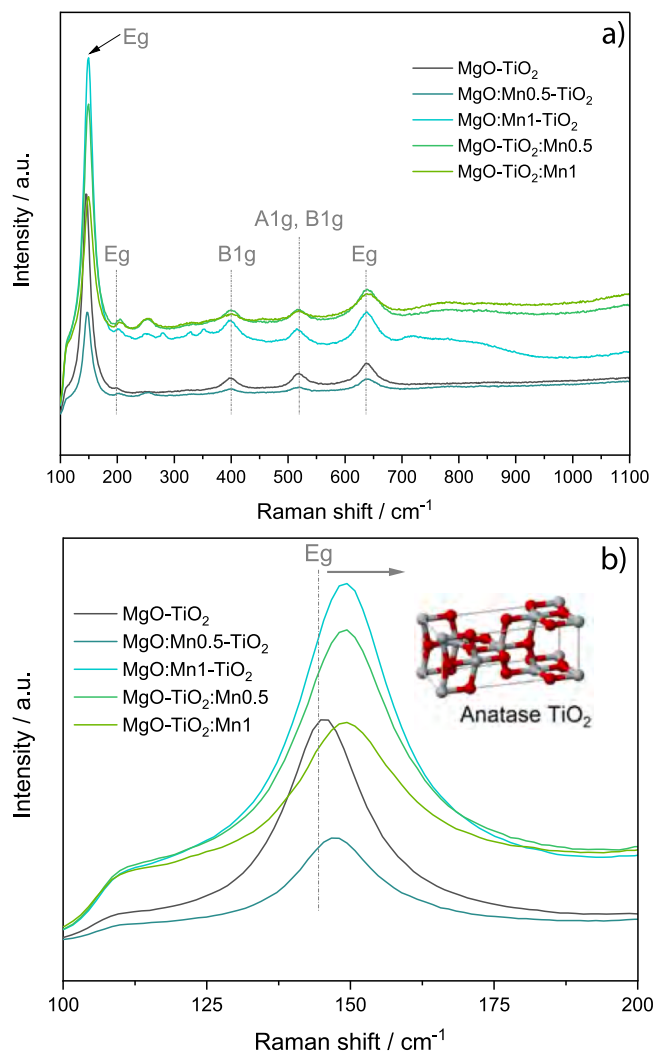

Fig. 2. First-order and second-order Raman spectra of the undoped and Mn-doped MgO − TiO$_2$ samples (λ = 532 nm) (a). The alterations in the vibration bands in the 100–1100 cm^{-1} range are given. Blueshift of the Raman band centered around 146 cm^{-1} (b).

and it is often linked to structural modifications within the material, such as defects, strain, or alterations in bonding [61]. For instance, introducing defects like vacancies, interstitials, or substitutions into a crystal lattice can modify the local bonding environment. If these defects strengthen bonds near the vibrational mode (e.g., by reducing bond lengths or increasing bond stiffness), the vibrational frequency rises, resulting in a blue shift. Defects can also induce lattice strain; compressive strain commonly leads to a blue shift by increasing the force constants of atomic bonds [62].

Furthermore, in nanoscale systems, defects can alter the size and shape of crystalline domains, contributing to quantum confinement
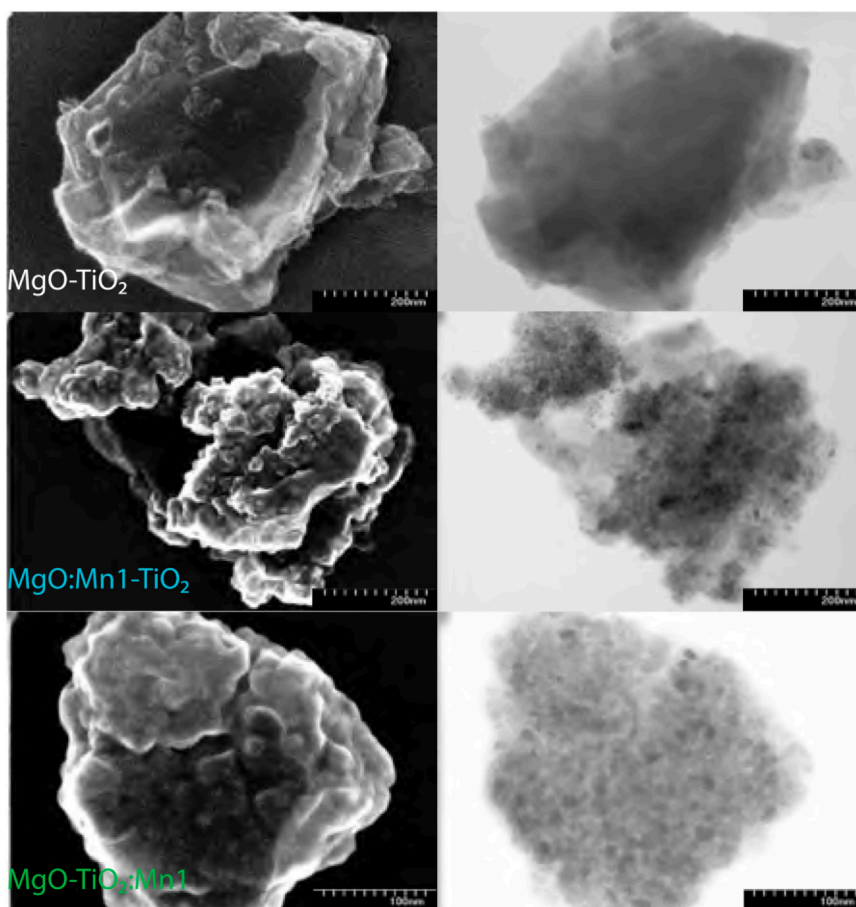
Fig. 3. SEM and TEM images of the undoped and 1% Mn-doped $MgO-TiO_2$ samples.

effects. These effects can enhance vibrational frequencies, leading to blue-shifted Raman peaks. For example, smaller grain sizes in materials such as ZnO and Si nanostructures have been reported to exhibit blue shifts due to the phonon confinement effect [63,64]. Additionally, defects may act as charge traps or modify the local electronic environment, thereby influencing electron-phonon interactions. Reduced electron-phonon coupling increases the energy of certain phonons, further contributing to blue shifts in Raman spectra [65].

SEM images presented in Fig. 3 show agglomerated structures. Together with the EDS measurements presented in Supplementary Fig. S-EDS the presence of the TiO_2 nanosized particles decorated on larger MgO particles is confirmed. The STEM analysis agrees well with the refinement results shown in Table 1 regarding the size of the particles present in the composites.

TiO_2 and MgO are known individually for their optical behavior [66,67]. Mahadevaiah et al. [66] reported emissions at $\lambda = 465$ nm from near-band emissions caused by electron-hole recombination in MgO. Moreover, Pallotti et al. [67] reported a wide peak emission of Rutile and Anatase TiO_2 in the green region around $\lambda = 530$ nm from Fabry-Perot fringes.

Previous works [68–70,61] demonstrated that combining EPR and PL spectroscopy is one of the most effective approaches for detecting and characterizing defect types in composite electrode materials. Each technique offers unique insights into defect structures, making their combined application particularly powerful. Some defect states exist as mid-gap states for semiconductors like ZnO, which have wide band gaps. These states can trap charge carriers and contribute to visible light emission, which PL spectroscopy detects. PL is especially sensitive to radiative recombination processes and can detect UV-emitting defect centers and visible emissions corresponding to specific mid-gap states, providing a broad spectrum of defect information.

On the other hand, EPR spectroscopy is highly specific to paramagnetic defects, such as unpaired electrons in dangling bonds or vacancy states. EPR can distinguish between surface and core defects based on their distinct electronic environments, which is achieved through changes in the shielding of defect states, reflected in variations of the g-factor. For example, deviations from the free electron g-factor (~ 2.0023) are caused by spin-orbit coupling effects, which reveal important details about defects' electronic structure and local symmetry. The challenge lies in the complementary nature of these techniques. While PL can detect a wide range of defect states (including non-paramagnetic ones), it provides limited structural information about defects' exact nature and spatial distribution.

Conversely, EPR is limited to paramagnetic centers, missing non-paramagnetic defects but excelling in providing precise details about the spin states, local coordination, and electronic environment of defects. By combining these techniques, we overcome these limitations. PL identifies various defect states and their optical activity, while EPR offers deeper insight into paramagnetic centers' electronic and magnetic properties. This dual approach provides a comprehensive understanding of defect types in composite electrode materials, enabling us to link specific defects to their roles in the material's electrochemical performance.

Supplementary Fig. S-PL shows the PL spectra of the undoped and Mn-doped $MgO-TiO_2$ samples, and Fig. 4 shows the peaks deconvolution for the undoped $MgO-TiO_2$ sample. The peak below 400 nm can be attributed to the MgO layer in the samples and the emissions in the UV range to the TiO_2 layer's near-band emissions between 400 and 450 nm. As reported previously, the rich emissions in the blue light range between 450 and 500 nm could be due to oxygen vacancy defects [71,72]. The major increase in the blue light range's intensity justifies the high specific capacitance in $MgO-TiO_2:Mn0.5$ sample due to
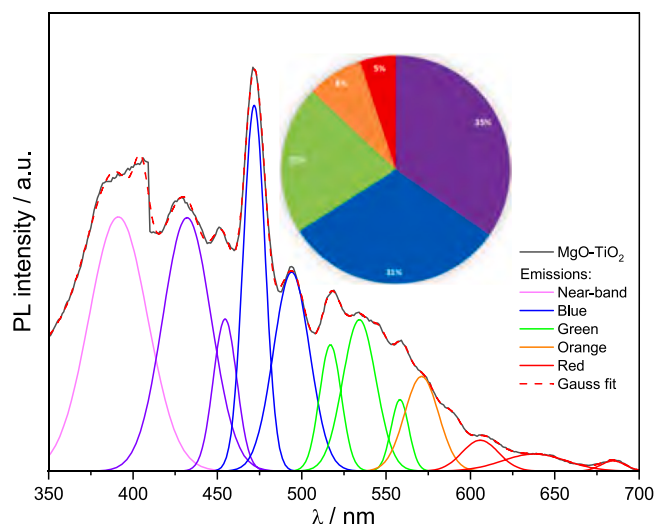
Fig. 4. Gaussian deconvolution of the undoped $MgO-TiO_2$ composite PL spectrum. PL = photoluminescence.

increasing active sites. Additionally, the lack of any major emissions in the red light range is expected due to the samples' absence of the $MgTiO_3$ and Mg_2TiO_4 phases, which have been reported to yield emissions in the red light range around 660–710 nm [73]. Considering the refinement results shown in Table 1 and the synthesizing conditions, there are no signs of the presence of $MgTiO_3$ and Mg_2TiO_4 phases. $MgTi_2O_5$ shows no major emissions unless perturbed by doping or creating oxygen vacancy defects by ultrasonic irradiation [58].

Moreover, the PL results complement the EPR results, reflecting the defects-rich $MgO-TiO_2$ samples. The pie chart in the inset of Fig. 4 displays the major emission peaks obtained from the Gaussian deconvolution. Around 35% of the emissions peaks originate from MgO, and near-band emissions of TiO_2 caused by electron-hole recombination. The remaining 31% are for blue emissions, and 21% are linked to defect-induced emissions, probably related to oxygen vacancies or interstitials [67,72,73]. The Gaussian fit for orange and red peaks emission can be ignored as no major peaks exist in that region.

Q-band EPR measurements were performed on all samples and are presented in Fig. 5. The undoped $MgO-TiO_2$ samples present an intense EPR signal with a g-value equal to 2.003 superimposed to two EPR signals much lower in intensity with $g = 2.0024$ and 2.0043. The first signal with characteristic $g = 2.003$ has been attributed to O^-
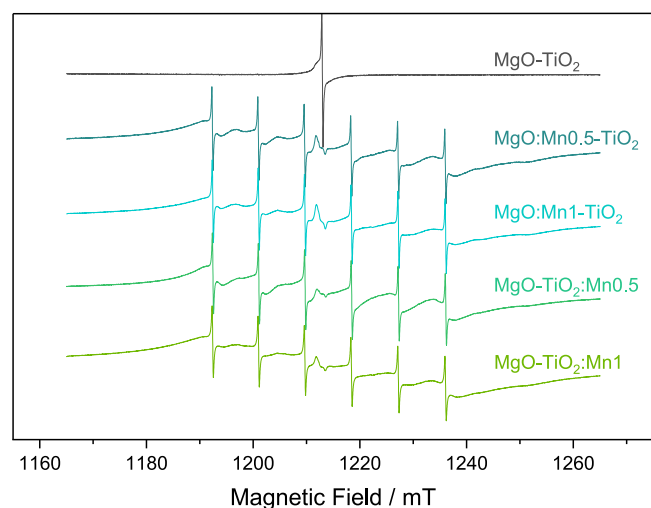

Fig. 5. EPR spectra of the undoped and Mn-doped $MgO-TiO_2$ samples in Q-band. EPR = electron paramagnetic resonance.

centers (hole centers) present in MgO. The second signal feature with the g value approximately equal to the free electron g-value has been attributed to electrons trapped at the material's surface [74]. The third EPR signal with $g = 2.0043$ is attributed to defects in the TiO_2 phase [75]. At the same time, it can be noticed that the Mn^{2+} EPR signal of the $MgO-TiO_2$:Mn1 sample is superimposed on a very broad signal, probably resulting from Mn ions agglomeration.

Indifferent which component of the composite was doped, MgO or TiO_2, the MgO related defect center with $g = 2.003$ vanishes, indicating that the Mn ions replace the MgO-related hole centers. All samples resemble a complex EPR signal composed of two different components. Given the nature of the composites and the annealing temperature of 400 °C, it is obvious that the Mn ions are diffusing through the composites, doping each component phase differently.

As shown in Fig. 5, the EPR signal comprises a sextet EPR line centered at $g \approx 2$, accompanied by less intense satellites. Such sextets are characteristic of the hyperfine interaction of unpaired electrons with the magnetic moment of a nuclear spin, $I = 5/2$ of the manganese nucleus ^{55}Mn ($I = 5/2$, 100% abundance). The EPR signals are assigned to Mn ions in different crystal phases presented in the $MgO-TiO_2$ composites. To verify the proposed models for the observed paramagnetic centers and determine their spin Hamiltonian parameters, the EPR spectra of the Mn-doped samples were simulated using the Easy-Spin simulation tool [76]. Mn atoms can substitute Mg or Ti sites in the $MgO-TiO_2$ composites crystal lattices. As a result, the paramagnetic Mn^{2+} ions with the electronic configuration $3d^5$ ($S = 5/2$) or Mn^{4+} ions with the electronic configuration $3d^3$ ($S = 3/2$) can be formed.

At higher magnetic fields, the spin states are close to pure S_z states (with z aligned along the direction of B_0), and only $m_s \longrightarrow m_s \pm 1$ transitions are allowed. The energy levels of the ground spin state of Mn ions (with the electron-spin quantum number $S > 1/2$) can be described by the spin Hamiltonian of the form:

$$H = \mu_B S_{Mn} \cdot \mathbf{g}_{Mn} \cdot B_0 + S \cdot \mathbf{A} \cdot I_{TM} + \sum_{k=2,4} \sum_{q=-k}^{k} B_k^q \mathbf{O}_k^q \qquad (1)$$

The first term shows the main electron Zeeman interaction. Here, μ_B denotes the Bohr magneton, B_0 the external magnetic field, and g the electronic g-matrix. The second term shows the hyperfine interaction, and in the last term, the interaction with local crystal fields is explained by the higher-order extended Stevens operators and the associated coefficients B_k^q, consisting of the conventional second-rank zero-field splitting parameters D and E, defined as $D = 3B_2^0$ and $E = B_2^2$ and fourth-rank F and a defined as $F = 180B_4^0 - 36B_4^4$ and $a = 24B_4^4$. All the used simulation parameters are summarized in Supplementary Table T-EPR, and the simulated spectrum is presented in Supplementary Fig. S-EPRsimu.

The simulations results show that the cubic MgO component was successfully doped with Mn^{2+} ions with $g = 2.001$, $A = 243$ MHz, $a = 87$ MHz, and $F = 12$ MHz, which is in good agreement with known paramagnetic Mn^{2+} center in MgO [77]. The second component has characteristic Mn^{2+} spin parameters with $g = 2.0008$, $A = 235$ MHz, and $D = 300$ MHz in a tetragonal environment of anatase TiO_2 [78]. At the same time, an EPR signal with a very large line width can be observed in the background of the Mn-doped samples, which we assigned to agglomerated Mn ions in the $MgTi_2O_5$ phase that is formed while decorating them MgO substrate with TiO_2 nanoparticles. The EPR spectroscopy analysis shows that the Mn ions diffuse through the composite doping each phase, while only Mn^{2+} ions are present in the resulting composite $MgO-TiO_2$ materials.

In this study, 5 symmetric SCs were designed using the undoped and Mn-doped $MgO-TiO_2$ composites as electrode materials, as described in the experimental section (see Scheme 2). Cyclic voltammetry (CV) measurements were performed at different scan rates (10, 20, 50, 100, and 200 mV/s) in the potential range of 0–1 V to analyze the composite's bare capacitive behavior. As shown in Fig. 6(a) and
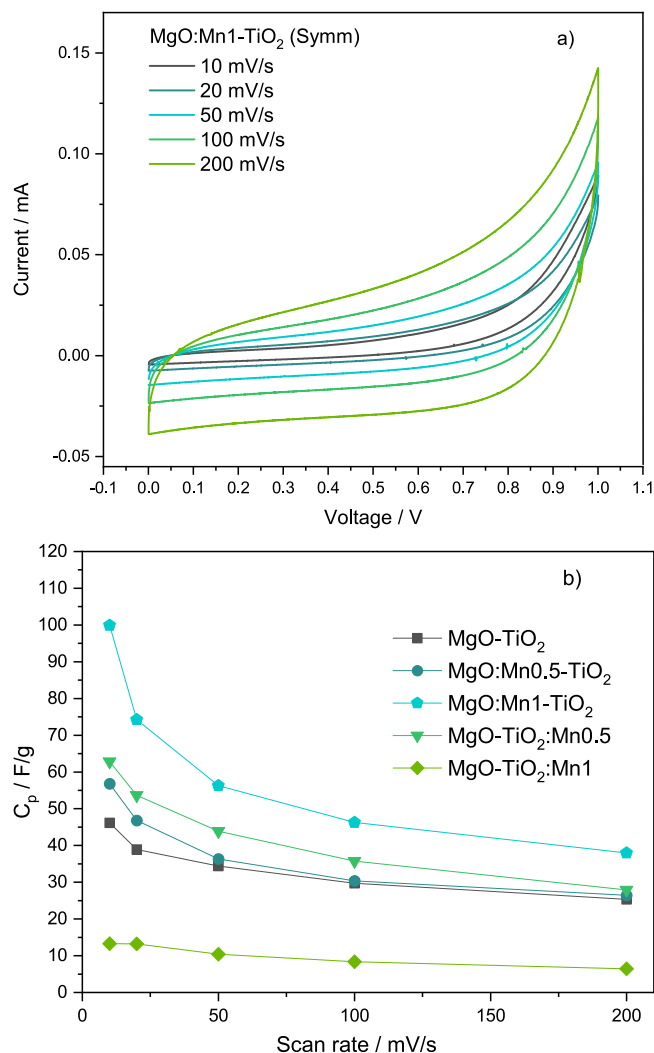
Fig. 6. CV diagrams (a), and specific capacitance obtained at different scan rates of the undoped and Mn-doped $MgO-TiO_2$ samples in symmetric SC devices. CV = cyclic voltammetry; SC = supercapacitor.

Fig. 7. CV diagrams (a), and specific capacitance obtained at different scan rates of the undoped and Mn-doped $MgO-TiO_2$ samples in asymmetric SC devices. CV = cyclic voltammetry; SC = supercapacitor.

Supplementary Fig. S-EP1, all voltammograms exhibited a quasi-rectangular shape, indicating pseudocapacitive behavior arising from fast and reversible redox reactions [12]. The specific capacitance (C_p) values were obtained employing the area encompassed by the voltammograms [54] and are summarized in Fig. 6(b). The SC prepared using the MgO:Mn1-TiO_2 sample displayed the highest performance, reaching the highest C_p value of 100 F/g at a 10 mV/s scan rate.

Comparing the C_p values of the undoped and Mn-doped $MgO-TiO_2$, it can be concluded that increasing the amount of Mn dopant in MgO and TiO_2 enhances the electrode's performance. Doping the MgO component with Mn^{2+}, as observed in the EPR section, has a higher impact on the composite from the C_p value point of view. While doping TiO_2 does not affect the composite behavior at low concentrations, the C_p value drops significantly by increasing the dopant concentration. Mn is a transition metal renowned for enhancing semiconductors' electrical properties, such as ZnO. Han et al. [79] reported that Mn-doped ZnO significantly improved electrical conductivity at high temperatures when compared with undoped ZnO.

The enhanced electrical performance due to doping affirms our findings, where PL spectra results also reveal a decrease in the intensity of emission peaks with increasing dopant percentage. Furthermore, the observed negative correlation between the scan rate and specific capacitance is attributed to the limited ion migration in the electrolyte due to shorter measurement times, affecting the redox reactions
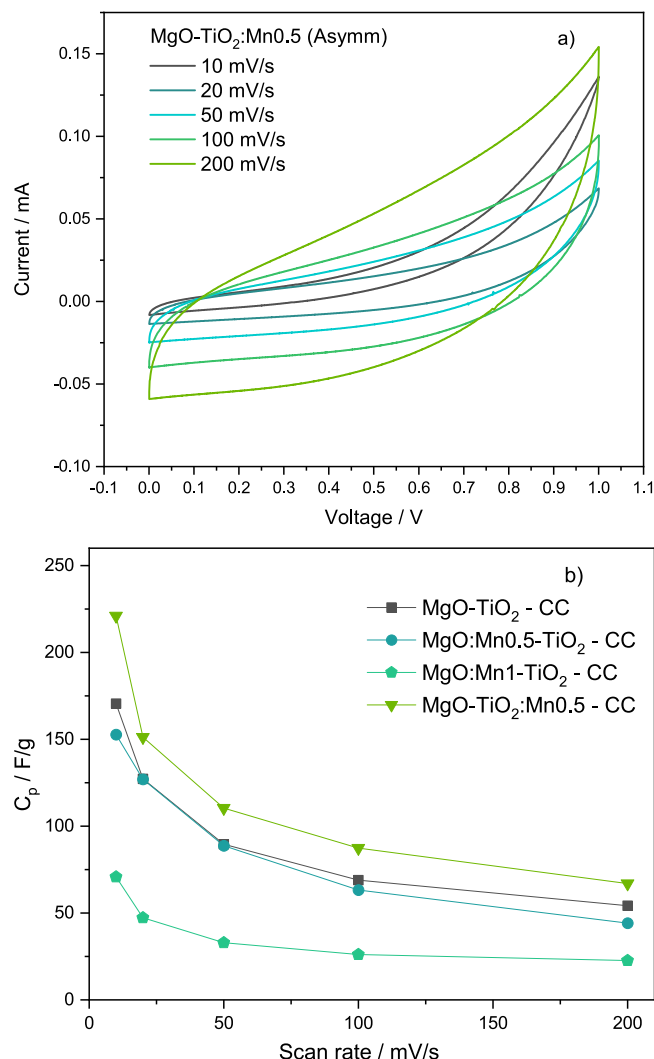
occurring at the electrode-electrolyte interface [54]. In other words, at slower scan rates, there is sufficient time for the facilitation of ion intercalations, and as such, higher capacitance values are obtained.

Further research was conducted by designing asymmetric SCs using undoped and Mn-doped $MgO-TiO_2$ samples (aside from the $MgO-TiO_2$:Mn1 sample) as electrode material since the symmetric SC prepared with this electrode material led to a C_p of 13 F/g and higher impedance compared to other electrode materials. Carbon from coffee waste [49] was used as the counter electrode material. Interestingly, as shown in Fig. 7(a), it was observed that the SC constructed from the $MgO-TiO_2$:Mn0.5 sample outperformed all other electrodes (see Fig. 7b), including MgO:Mn1-TiO_2, yielding the highest C_p value of 221 F/g at 10 mV/s. All the CV curves are presented in Supplementary Figs. S-EP1 and S-EP2. In the comparative analysis with the undoped $MgO-TiO_2$, adding 0.5% Mn into TiO_2 improved the performance. However, as the Mn dopant concentration was further increased, an adverse impact on the performance was observed. In addition, it can be concluded that $MgO-TiO_2$:Mn0.5 has a better synergy with carbon obtained from coffee. The improvement of electrochemical performance post combining the material with carbon from coffee waste in asymmetric SC devices could be attributed to many factors. Carbon's relatively high surface area significantly increases the devices' specific capacitance. Additionally, the synergy between the asymmetric materials and the electrolyte plays a crucial role in ion transportation. These
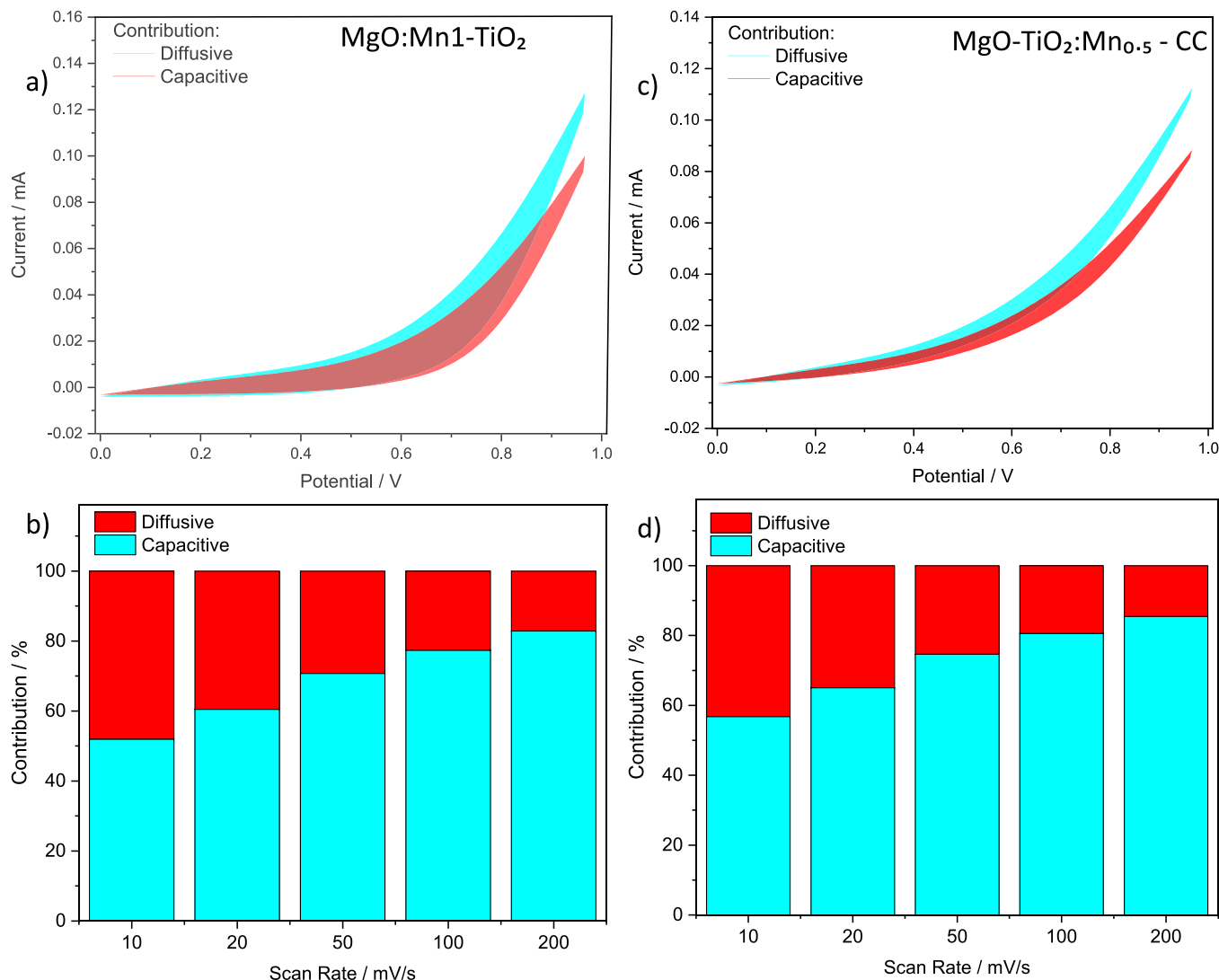
Fig. 8. Capacitive and diffusive regions of the CV curve measured with a scan rate of 10 mV/s (a) and (c), and the capacitive and diffusive contributions at different scan rates (b) and (d) calculated for the best working symmetric (MgO:Mn1-TiO$_2$) and asymmetric (MgO − TiO$_2$:Mn0.5 - CC) SC devices. CC = coffee-waste-derived carbon; CV = cyclic voltammetry; SC = supercapacitor.

results are further understood by analyzing the working mechanism of the SC devices by running Dunn's technique.

The working mechanism of both symmetric and asymmetric SCs show similar behavior at high scan rates, as shown in Figs. 8(a–d). At higher scan rates, the capacitive contribution dominates the mechanism, indicating that the mechanism is mostly an EDLC type involving the physical transport of ions between the electrodes. However, as the scan rate decreases, the system shows a 50:50 contribution of both EDLC and pseudocapacitive mechanisms, indicating both physical transport and rapid redox reactions between the electrodes. This behavior is related to the availability of sufficient time for chemical reactions to take place at lower scan rates.

The impedance of symmetric and asymmetric SCs was evaluated using EIS by applying an alternating current and plotting the real impedance against the negative imaginary impedance on a Nyquist diagram. In the existing literature, the x-intercept of the Nyquist plot in the high-frequency region is commonly associated with internal resistance or equivalent series resistance (ESR), which is a combination of the electrode and electrolyte resistance and the resistance at the interface between the electrode and current collector, known as contact resistance [37,80]. Additionally, the curvature's diameter observed in the Nyquist plot's high-frequency region (see Supplementary Fig. S-PEIS) is related to the charge transfer resistance (R_{ct}). In contrast, the linear slope in the low-frequency region is linked to the

Warburg impedance. The Warburg element, also known as the transmissive diffusion element, is associated with the diffusion of ions within the electrode material and electrolyte. It is crucial in SC performance and cycling stability in symmetric and asymmetric SC devices. The Z-fit results show the lowest value for the Warburg element coefficient for the highest performance symmetric and asymmetric SC devices, which indicates sufficient ion transportation and lack of polarization caused by sluggish transportation of ions. Additionally, a well-maintained Warburg element suggests a stable interface between the electrode materials and the electrolyte, which contributes to improving the cyclic stability of the SC devices by reducing degradation [54,81].

Figs. 9(a) and (b) show the Nyquist plots of the symmetric and asymmetric SCs and the corresponding Z-Fits. The inset of the figures presents the equivalent circuit used for the fitting. The values of the equivalent circuit components obtained after fitting are summarized in Supplementary Table T-PEIS. Given that the R_1 values of the equivalent circuits closely align with the x-intercepts of the Nyquist plots, it is reasonable to suggest that these values correspond to the internal resistance of the SCs. As can be seen in Supplementary Table T-PEIS, the MgO:Mn1-TiO$_2$ sample, which has the highest C_p value among the symmetric SCs, has the lowest internal resistance of 0.189 Ω.

Similarly, the MgO − TiO$_2$:Mn0.5 sample with the highest C_p value among the asymmetric SCs has the lowest internal resistance of 0.127
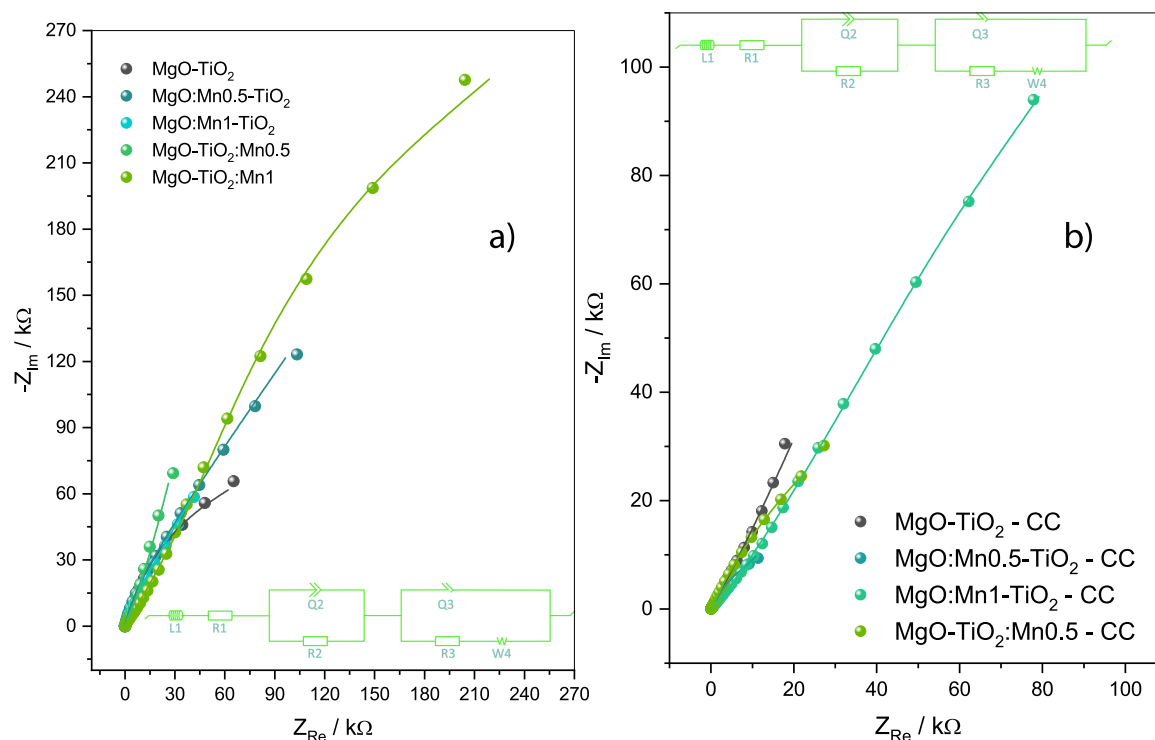
Fig. 9. Impedance measurements (Nyquist Plot) and Z-fit of the undoped and Mn-doped $MgO-TiO_2$ samples in symmetric (a) and asymmetric (b) SC devices. The inset presents the equivalent circuit used for fitting. SC = supercapacitor.

Ω. No semicircles were observed in the high-frequency zone, indicating minimal charge transfer resistance and rapid ion diffusion. The slope of the linear part in the low-frequency zone is similar in all Nyquist plots, representing that the SCs have a close Warburg resistance (W). Furthermore, the constant phase element (Q) was observed in all equivalent circuits, indicating the degree to which the capacitors deviate from the ideal capacitance [37,54]. Nevertheless, the small and negligible values of the constant phase elements suggest that the SCs demonstrate a behavior close to ideal capacitance.

Among the symmetric SCs, the device prepared with the MgO:Mn1-TiO$_2$ sample exhibited the lowest impedance value, further supporting the high specific capacitance value achieved with MgO:Mn1-TiO$_2$. Similarly, the lowest impedance value for all asymmetric SCs was found to belong to the SC prepared with $MgO-TiO_2$:Mn0.5, which correlates negatively with the calculated specific capacitance value, attributed to lower impedance values facilitating a more effortless, rapid ion transfer and diffusion across the electrode-electrolyte interface, consequently leading to improved C_p and overall SC performance.

The galvanostatic charge-discharge potential limitation (GCPL) technique was employed in the potential range of -1 to $+1$ V to assess the electrochemical stability of the $MgO-TiO_2$ samples; the results are presented in Supplementary Fig. S-GCPL. The GCPL graph slightly deviates from the symmetric triangular shape, indicating Faradaic redox reactions. These observations agree with the previous analysis of the working mechanism. The obtained data was utilized to plot the capacity retention and voltage holding graphs. Fig. 10 illustrates the cyclic stability of symmetric SCs by plotting capacity retention against cycle number. Remarkably, it was found that all symmetric SCs showed high stability with capacity retention of over 86% sustained up to 1000 cycles. The symmetric SC with MgO:Mn1-TiO$_2$ could retain more than 90% of its capacity throughout 1000 cycles. Similarly, the asymmetric SC utilizing $MgO-TiO_2$:Mn0.5 exhibited an impressive capacity retention of over 92%. In some cases, the values of the capacity retention exceeded 100%, which can be a consequence of some chemical activation processes indicating pseudocapacitive behavior, as shown in Figs. 8(a–d). Moreover, the voltage holding graphs exhibited high

stability of the SCs, with no sharp decline in performance as presented in Fig. 11. The highest performance sample prepared with $MgO-$TiO$_2$:Mn0.5 and coffee-waste-derived carbon (CC) exhibited the lowest IR drop and maintained the highest potential value of 0.3 V throughout the voltage holding test.

The symmetric SC with MgO:Mn1-TiO$_2$ and the asymmetric SC utilizing $MgO-TiO_2$:Mn0.5 exhibited the best electric properties, which can be related to the characteristics observed in the XRD, PL, and EPR spectroscopy measurements. The multiphasic nature of the material plays a crucial role in the working mechanism of the SC device. For the asymmetric SC devices, the higher MgTi$_2$O$_5$ content of 55% enhances ion storage and redox activity by increasing charge transfer when combined with the carbon-based material that offers a high surface area for the EDLC mechanism to take place [88]. These results agree with the Dunn results, which display a higher capacitive working mechanism that relies on increased surface area due to using carbon-based material. As for the symmetric SC devices, the 40% content of MgTi$_2$O$_5$ most likely strikes a balance through providing faradaic redox-reactions active sites, which is reflected through the results of Dunn analysis that reveals a higher diffusive phase that involves faradaic redox-reactions. The major increase in the intensity of the blue light range justifies the high specific capacitance in the $MgO-TiO_2$:Mn0.5 sample due to increased active sites. Oxygen vacancies are well known to increase the performance in SC devices due to increasing the conductivity and providing more active sites for electrochemical reactions, thus boosting the capacitance Wang et al. [89]. As for the symmetric SCs, the synergy between the electrode materials in MgO:Mn1-TiO$_2$ seems dominated by the rich near-band emissions. At the same time, the increased performance of these composites is associated with the low intrinsic defect concentration of the $MgO-TiO_2$ material, where the EPR signal with $g = 2.003$ attributed to O^- centers (hole centers) present in MgO vanishes and the other two with $g = 2.0024$ and 2.0043 attributed to electrons trapped at the MgO's surface and defect centers in TiO$_2$ have the lowest intensity as compared to the Mn^{2+} ions signal, indicating that the presence of these ions in the materials enhance its eclectic properties. At the same time, the clustering of the doping ions, as observed in $MgO-TiO_2$:Mn1, negatively influences the electric properties.
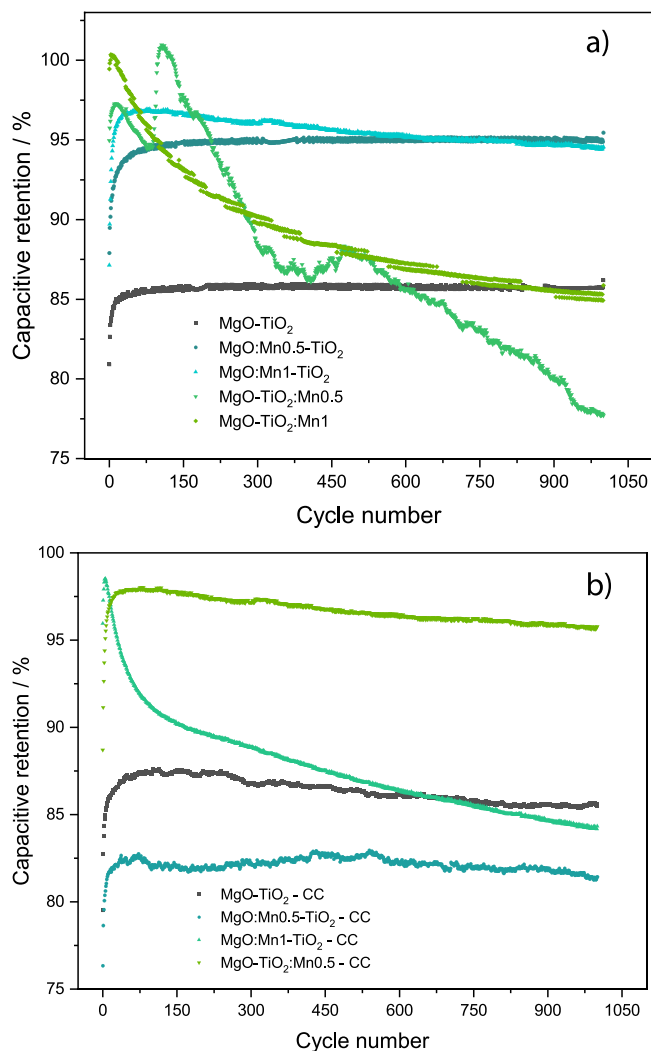
Fig. 10. Charge retention of the undoped and Mn-doped MgO−TiO$_2$ composites in symmetric and asymmetric SC devices. SC = supercapacitor.
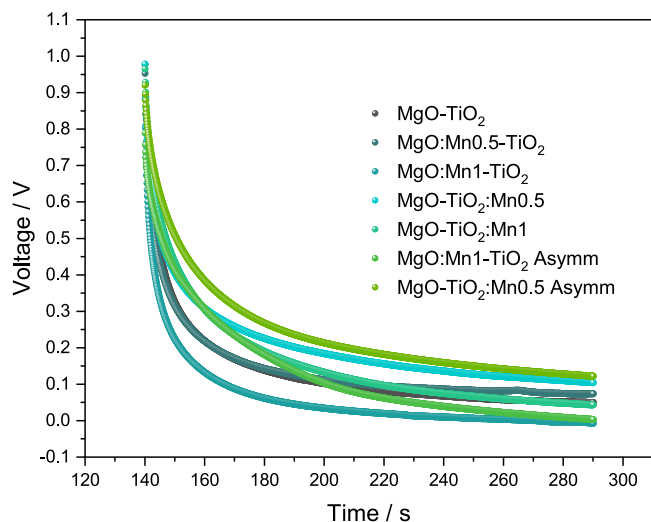

Fig. 11. Voltage holding test of the undoped and Mn-doped MgO−TiO$_2$ samples used as electrode materials in symmetric and asymmetric SC devices. SC = supercapacitor.

Mn as a TM dopant in MO electrodes such as MgO and TiO$_2$ has been reported as the best 3d TM dopant due to the production of intermediate donor states inside the forbidden gaps with fewer defected sites

and the enhancement of charge mobility. Ojha et al. [33] investigated mesoporous Mn-doped TiO$_2$ nanoparticles synthesized via the sol-gel route. They found that Mn doping improved the mesoporosity and created more active sites, ultimately leading to incredible capacitive performance. Furthermore, Naffouti et al. [90] utilized a spray pyrolysis technique to design Mn-doped TiO$_2$ thin films to explore structural, morphological, and optical properties. They show that more defects were produced within the forbidden band as the Mn doping concentration increased. Consequently, the indirect energy band gap dropped from a maximum of 3.45 eV to a minimum of 3.38 eV. They justified such a desirable drop in band gap energy due to an increased structural disorder, a larger number of crystal lattice defects, and the introduction of tail states at band edges – all of which directly cause Urbach energy widening and band gap shrinkage associated with Mn-doping. Their results were further supported by XRD analysis of the thin film morphologies and seemed to be in perfect agreement with a similar behavior encountered in yet another study led by Lin et al. [91], where they investigated multivalent Mn-doped TiO$_2$ thin films. GCPL plots provided in Supplementary Fig. S-GCPL conclude the results as mentioned above. Amongst the symmetric and asymmetric SC devices, MgO:Mn1-TiO$_2$ and MgO−TiO$_2$:Mn0.5, respectively, showed the highest charge-discharge time, indicating the highest capacity, and energy density, along with the lowest resistivity.

Comparing these results to similar materials like ZnO–CoO$_3$ proposed by Mishra et al. [82], where the SC maintained a potential of 0.4 V in a symmetric design. Herein, we obtained a slightly smaller value of that, but with the advantage of using a green source for carbon with a boosted specific capacitance value of 221 F/g. Moreover, the overall power density and energy density of the designed SCs are shown in Fig. 12 and Table 2. The performance was compared to similar materials presented in the literature, showing that the coffee-waste-derived carbon-enhanced SC device shows promising potential regarding its specific capacitance and power density while the energy density value is in good parameters. [83] used TiO$_2$–CuSe composites in combination with active carbon, reaching comparable specific capacity values (184 F/g) but much lower energy and power densities. Karthikeyan et al. [84] used a MgO-based material combined with AC and achieved 66 F/g specific capacity value, which is ~3 times lower than the value obtained in this study for the Mn-doped MgO−TiO$_2$ composites boosted with CC. At the same time, the energy densities are in the same range ~30 Wh/kg. Thus, the proposed composite material based on Mn-doped MgO−TiO$_2$ boosted by coffee-waste-derived carbon shows great potential in the green SC energy storage field. There
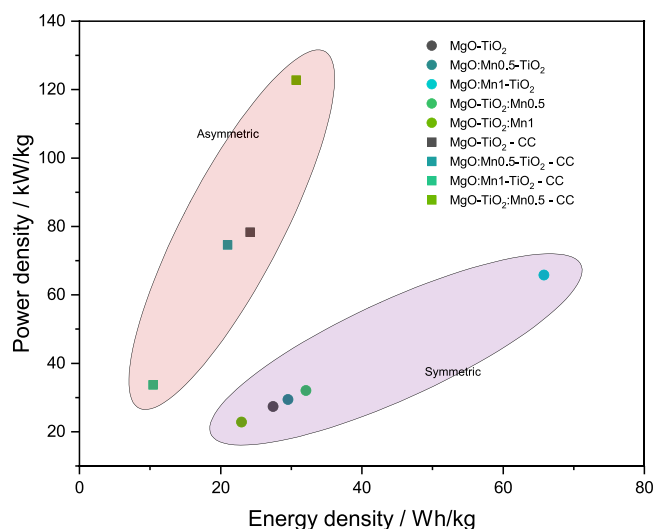

Fig. 12. Ragone plot showing the Power density versus the Energy density of the symmetric and asymmetric SC devices based on undoped and Mn-doped MgO−TiO$_2$ composites. SC = supercapacitor.

Table 2

Specific capacitance, energy, and power density values for different materials presented in the literature and the best values obtained in this study

Electrodes materials	SC Type	C_p F/g	Energy density Wh/kg	Power density kW/kg	Ref.
MgO:Mn1-TiO$_2$	symm	100	14	65.8	This work
MgO$-$TiO$_2$:Mn0.5	CC	221	30.7	122.8	This work
ZnO$-$CoO$_3$	symm	177	39	19.4	[82]
TiO$_2$$-$CuSe	AC	184	27	7.1	[83]
MgO-V	symm	50	4.2	-	[12]
MgO-MWCNT	AC	66	30	-	[84]
3DG-SnO$_2$–TiO$_2$	AC	92	28.6	-	[85]
TiO$_2$/CDC	CDC	173	10.8	-	[86]
RuO$_2$/TiO$_2$	AC	46	5.7	-	[87]

Cp = specific capacitance; SC = supercapacitor.

could be several factors behind the improved electrochemical performance of MgO$-$TiO$_2$ in comparison to MgO and TiO$_2$ based SC devices. First, the composite multiphasic nature of MgO$-$TiO$_2$ material could improve the performance through the optimized surface properties and electronic structure. In addition to that, oxygen vacancies in MgO$-$TiO$_2$ are more probable to form than in TiO$_2$ and MgO, which also contributes to boosting the electrochemical performance of the SC device [92].

4. Conclusions

Although utilizing MgO and TiO$_2$, particularly in energy storage applications, has not been thoroughly discussed in the literature, recent studies highlighted the tremendous potential of employing composite metal oxides as electrode materials in hybrid SCs. The morpho-structural characterization carried out with various spectroscopic techniques showed the presence of Anatase TiO$_2$ phase and MgTi$_2$O$_5$ as the main phases in all Mn-doped and undoped MgO$-$TiO$_2$ samples. The MgTi$_2$O$_5$ phase consists of an orthorhombic crystal structure, accompanied by a tetragonal structure of the Anatase TiO$_2$ phase and a cubic structure of MgO. The results were sustained by Ramana spectroscopy, where it was observed that doping the anatase TiO$_2$ phase with Mn ions induces a blue shift, which typically reflects changes in the vibrational energy of molecular or lattice modes often linked to structural modifications within the material. The PL measurements show that around 35% of the emissions peaks originate from MgO and that the near band emissions of TiO$_2$ are caused by electron-hole recombination. The remaining 31% are for blue emissions, and 21% are linked to defect-induced emissions, probably related to oxygen vacancies or interstitial. The simulations on the Q-band EPR spectra show three different components originating from various systems. One is given by the cubic MgO doped with Mn^{2+} ions. The second component shows characteristic Mn^{2+} spin parameters compared to anatase TiO$_2$. At the same time, an EPR signal with a very large line width can be observed in the background of the Mn-doped samples, which is assigned to agglomerated Mn ions in the MgTi$_2$O$_5$ phase that is formed. The EPR spectroscopy results show that the Mn ions diffuse through the composite, doping each phase, while only Mn^{2+} ions are present in the resulting composite MgO$-$TiO$_2$ materials.

Higher capacitance values, lower impedances, and improved electrical conductivities were achieved upon growing TiO$_2$ on MgO nanoparticles and decorating the core-shell structure with Mn-dopant to produce composite electrodes while constructing the counter-electrode from coffee-waste-derived carbon. It is worth mentioning that doping the MgO$-$TiO$_2$ composites with Mn enhanced the overall electrical properties, making it possible to use them as electrode material in symmetric SC devices with no additional booster material yet reaching a maximum specific capacitance of 100 F/g at a 10 mV/s scan rate, an energy density of 14 Wh/kg and power density of 65.8 kW/kg.

When using coffee-waste-derived carbon as a booster, promising results were achieved for the MgO$-$TiO$_2$:Mn0.5 composite with

excellent capacitance behavior between 0 and 1 V at low scan rates, delivering a maximum specific discharge capacitance of 221 F/g at a 10 mV/s scan rate, an energy density of 221 Wh/kg, and power density of 122.78 kW/kg The enhanced performance of such SCs is mainly due to the synergy between MgO, TiO$_2$, and the carbon-based material, all enhanced by the induced Mn^{2+}-based defects that were analyzed employing EPR spectroscopy. Consequently, the low cost, abundance, and purity of MgO and TiO$_2$, combined with the sustainable biomass-derived carbon, and considering the high capacitance and energy density values obtained, empower the possibility of using them in practical energy applications.

CRediT authorship contribution statement

Mohamad Hasan Aleinawi: Conceptualization, Methodology, Validation, Formal analysis, Investigation, Writing - Original Draft, Writing - Review & Editing, Visualization. **Maria Stefan:** Formal analysis, Methodology, Investigation, Investigation, Writing - Original Draft, Writing - Review & Editing, Visualization. **Eminenur Saritas:** Formal analysis, Investigation, Data Curation, Writing - Original Draft, Writing - Review & Editing, Visualization. **Abdalla Hroub:** Formal analysis, Investigation, Writing - Original Draft, Visualization. **Feray Bakan-Misirlioglu:** Formal analysis, Investigation,Writing - Original Draft, Visualization. **Sergiu Macavei:** Formal analysis, Investigation. **Lucian Barbu Tudoran:** Formal analysis, Investigation. **Kuray Dericiler:** Formal analysis, Investigation. **Burcu Saner Okan:** Formal analysis, Investigation. **Emre Erdem:** Conceptualization, Validation, Formal analysis, Resources, Data Curation, Writing - Original Draft, Writing - Review & Editing, Visualization, Supervision, Funding acquisition. **Arpad Mihai Rostas:** Conceptualization, Methodology, Validation, Formal analysis, Investigation, Resources, Data Curation, Writing - Original Draft, Writing - Review & Editing, Visualization, Supervision, Funding acquisition.

Declaration of Competing Interest

The authors declare that they have no known competing financial interests or personal relationships that could have appeared to influence the work reported in this paper.

Acknowledgments

Appendix A. Supporting material

Supplementary data associated with this article can be found in the online version at doi:10.1016/j.nxener.2025.100238.

References

[1] J. Castro-Gutiérrez, A. Celzard, V. Fierro, Energy storage in supercapacitors: focus on tannin-derived carbon electrodes, Front. Mater. 7 (2020) 217.

[2] A. Afif, S.M. Rahman, A.T. Azad, J. Zaini, M.A. Islan, A.K. Azad, Advanced materials and technologies for hybrid supercapacitors for energy storage–a review, J. Energy Storage 25 (2019) 100852.

[3] S. Najib, E. Erdem, Current progress achieved in novel materials for supercapacitor electrodes: mini review, Nanoscale Adv. 1 (2019) 2817–2827.

[4] A.U. Ammar, I.D. Yildirim, F. Bakan, E. Erdem, ZnO and MXenes as electrode materials for supercapacitor devices, Beilstein J. Nanotechnol. 12 (2021) 49–57.

[5] Z.S. Rozveh, M. Moradi, M. Keyhan, V. Safarifard, P. Yaghoubizadeh, M.J. Eshraghi, The electrochemical performance of gallium nitride composited with g-c₃n₄ in bulk and oxidized forms for supercapacitors, Synth. Met. 307 (2024) 117686.

[6] Z.S. Iro, C. Subramani, S. Dash, et al., A brief review on electrode materials for supercapacitor, Int. J. Electrochem. Sci. 11 (2016) 10628–10643.

[7] P. Simon, Y. Gogotsi, Materials for electrochemical capacitors, Nat. Mater. 7 (2008) 845–854.

[8] B. Chameh, M. Pooriraj, M. Keyhan, M. Moradi, Cu-MOF-derived CuO/NiO/Ni₃(VO₄)₂ composite materials with improved electrochemical performance for supercapacitor, J. Mater. Sci.: Mater. Electron. 34 (2023) 525.

[9] A. Kanwade, P.M. Shirage, et al., A review on synergy of transition metal oxide nanostructured materials: effective and coherent choice for supercapacitor electrodes, J. Energy Storage 55 (2022) 105692.

[10] B. Chameh, M. Moradi, S. Hajati, Co-electrophoretic deposition of Mn₂O₃/activated carbon on cuo nanowire array growth on copper foam as a binder-free electrode for high-performance supercapacitors, J. Mater. Sci.: Mater. Electron. 32 (2021) 27268–27278.

[11] J. Hornak, Synthesis, properties, and selected technical applications of magnesium oxide nanoparticles: a review, Int. J. Mol. Sci. 22 (2021) 12752.

[12] A. Hroub, M.H. Aleinawi, M. Stefan, M. Mihet, A. Ciorita, F. Bakan-Misirlioglu, E. Erdem, A.M. Rostas, Vanadium-doped magnesium oxide nanoparticles as electrodes in supercapacitor devices, J. Alloy. Compd. 958 (2023) 170442.

[13] R.G. Bobade, N.B. Dabke, S.F. Shaikh, B.J. Lokhande, R.S. Mane, R.C. Ambare, Facile chemical synthesis of BaO: Mgo nanorods for designing distinctive solid-state asymmetric supercapacitor device with activated carbon, J. Energy Storage 84 (2024) 110776.

[14] D. Gaikwad, R. Bobade, V. Suryawanshi, U. Nakate, S. Shaikh, A.M. Al-Enizi, N. Dabke, B. Lokhande, R.C. Ambare, Electrochemical property of nanosphere-like MgO electrode synthesized via silar in asymmetric supercapacitor, J. Mater. Sci.: Mater. Electron. 35 (2024) 363.

[15] V.B. Suryawanshi, R.G. Bobade, D.S. Gaikwad, U.T. Nakate, S.F. Shaikh, B.J. Lokhande, R.C. Ambare, Nano-architectured BaO thin film electrode synthesized via silar technique for supercapacitor application, Chem. Pap. 78 (2024) 4689–4697.

[16] N. Pathak, R. Kadam, S. Mukherjee, Defect and dopant mediated optical properties in LiNbO₃ and Eu³⁺: LiNbO₃, in: Proceedings of the Seventh DAE-BRNS Interdisciplinary Symposium on Materials Chemistry, 2018.

[17] A. Kozlovsky, M. Zdorovets, Effect of doping of Ce⁴⁺/³⁺ on optical, strength and shielding properties of (0.5-x)TeO₂-0.25 MoO-0.25Bi₂₋ₓCeO₂ glasses, Mater. Chem. Phys. 263 (2021) 124444.

[18] V. Suryavanshi, R. Bobade, B. Lokh, R. Ambare, et al., Electro-synthesized bismuth oxide nanomaterials on flexible substrate electrode for supercapacitor application, ES Energy Environ. 21 (2023) 944.

[19] Y. Sun, N. Huang, D. Zhao, X. Wang, J. Zhang, S. Liu, L. Guo, X. Sun, Microwave-assisted in-situ isomorphism via introduction of Mn into CoCo₂O₄ for battery-supercapacitor hybrid electrode material, Chem. Eng. J. 430 (2022) 132729.

[20] K. Fang, Q. Xie, C. Wang, X. Qiu, Y. Wang, W. Yang, X.-w. Yu, Understanding the feasibility of manganese substitution for cobalt in the synthesis of nickel-rich and cobalt-free cathode materials, ACS Appl. Energy Mater. 4 (2021) 7190–7200.

[21] V. Kuraganti, A. Jain, R. Bar-Ziv, A. Ramasubramaniam, M. Bar-Sadan, Manganese doping of MoSe₂ promotes active defect sites for hydrogen evolution, ACS Appl. Mater. Interfaces 11 (2019) 25155–25162.

[22] J. Yuan, D. Yao, L. Jiang, Y. Tao, J. Che, G. He, H. Chen, Mn-doped NiMoO₄ mesoporous nanorods/reduced graphene oxide composite for high-performance all-solid-state supercapacitor, ACS Appl. Energy Mater. 3 (2020) 1794–1803.

[23] Z. Zhang, H. Huo, L. Wang, S. Lou, L. Xiang, B. Xie, Q. Wang, C. Du, J. Wang, G. Yin, Stacking fault disorder induced by Mn doping in Ni(OH)₂ for supercapacitor electrodes, Chem. Eng. J. 412 (2021) 128617.

[24] F. Lu, Y. Ji, D. Shi, J. Yao, L. Pei, Electrochemically activated 3D Mn doped NiCo hydroxide electrode materials toward high-performance supercapacitors, J. Colloid Interface Sci. 641 (2023) 510–520.

[25] Y. Wang, D. Yan, S. El Hankari, Y. Zou, S. Wang, Recent progress on layered double hydroxides and their derivatives for electrocatalytic water splitting, Adv. Sci. 5 (2018) 1800064.

[26] H. Li, Z. Chen, C.K. Tsang, Z. Li, X. Ran, C. Lee, B. Nie, L. Zheng, T. Hung, J. Lu, et al., Electrochemical doping of anatase TiO₂ in organic electrolytes for high-performance supercapacitors and photocatalysts, J. Mater. Chem. A 2 (2014) 229–236.

[27] J. Li, J. Ao, C. Zhong, T. Yin, Three-dimensional nanobranched TiO₂-carbon nanotube for high performance supercapacitors, Appl. Surf. Sci. 563 (2021) 150301.

[28] R. Lakra, R. Kumar, D. Thatoi, A. Soam, et al., Synthesis of TiO₂ nanoparticles as electrodes for supercapacitor, Mater. Today.: Proc. 74 (2023) 863–866.

[29] Z.-K. He, Y. Lu, C. Zhao, J. Zhao, Z. Gao, Y.-Y. Song, Surface-charge regulated TiO₂ nanotube arrays as scaffold for constructing binder-free high-performance supercapacitor, Appl. Surf. Sci. 567 (2021) 150832.

[30] H. Wu, D. Li, X. Zhu, C. Yang, D. Liu, X. Chen, Y. Song, L. Lu, High-performance and renewable supercapacitors based on TiO₂ nanotube array electrodes treated by an electrochemical doping approach, Electrochim. Acta 116 (2014) 129–136.

[31] M. Rehan, X. Lai, G.M. Kale, Hydrothermal synthesis of titanium dioxide nanoparticles studied employing in situ energy dispersive X-ray diffraction, CrystEngComm 13 (2011) 3725–3732.

[32] X. Ning, X. Wang, X. Yu, J. Zhao, M. Wang, H. Li, Y. Yang, Outstanding super-capacitive properties of Mn-doped TiO₂ micro/nanostructure porous film prepared by anodization method, Sci. Rep. 6 (2016) 22634.

[33] D.P. Ojha, M.B. Poudel, H.J. Kim, Investigation of electrochemical performance of a high surface area mesoporous Mn-doped TiO₂ nanoparticle for a supercapacitor, Mater. Lett. 264 (2020) 127363.

[34] B. YükselPrice, G. Hardal, M. Açıkgöz, S. Repp, E. Erdem, Effects of MnO doping on the electronic properties of zinc oxide: 406 ghz electron paramagnetic resonance spectroscopy and newman superposition model analysis, J. Appl. Phys. 118 (2015) 175705.

[35] S. Yildirimcan, K. Ocakoglu, S. Erat, F.M. Emen, S. Repp, E. Erdem, The effect of growing time and Mn concentration on the defect structure of ZnO nanocrystals: X-ray diffraction, infrared and EPR spectroscopy, RSC Adv. 6 (2016) 39511–39521.

[36] H. Kaftelen, D.E. Kanar, S. Repp, S. Weber, E. Erdem, Investigation of Mn-doped sodium-potassium niobate ((K, Na) NbO₃) ceramics by epr and impedance spectroscopic methods, Ferroelectrics 494 (2016) 11–18.

[37] A.U. Ammar, F. Bakan-Misirlioglu, M.H. Aleinawi, G. Franzo, G.G. Condorelli, F.N.T. Yesilbag, Y.O. Yesilbag, S. Mirabella, E. Erdem, All-in-one supercapacitors with high performance enabled by Mn/Cu doped ZnO and MXene, Mater. Res. Bull. 165 (2023) 112334.

[38] A.U. Ammar, I.D. Yildirim, M.H. Aleinawi, M. Buldu-Akturk, N.S. Turhan, S. Nadupalli, A.M. Rostas, E. Erdem, Multifrequency EPR spectroscopy study of Mn, Fe, and Cu doped nanocrystalline ZnO, Mater. Res. Bull. 160 (2023) 112117.

[39] P.H. Patil, V.V. Kulkarni, S.A. Jadhav, An overview of recent advancements in conducting polymer–metal oxide nanocomposites for supercapacitor application, J. Compos. Sci. 6 (2022) 363.

[40] V. Sunil, R. Jose, Hybrid Nanocomposite Metal Oxide Materials for Supercapacitor Application, Chemically Deposited Nanocrystalline Metal Oxide Thin Films: Synthesis, Characterizations, and Applications, Springer, Switzerland, 2021, pp. 673–724.

[41] J. Selinger, S. Stock, W. Schlemmer, M. Hobisch, N. Kostoglou, Q. Abbas, O. Paris, C. Mitterer, M. Hummel, S. Spirk, Nanoporous carbon electrodes derived from coffee side streams for supercapacitors in aqueous electrolytes, Nanomaterials 12 (2022) 2647.

[42] K. Pandey, H.K. Jeong, Coffee waste-derived porous carbon based flexible supercapacitors, Chem. Phys. Lett. 809 (2022) 140173.

[43] Y. Gong, D. Li, C. Luo, Q. Fu, C. Pan, Highly porous graphitic biomass carbon as advanced electrode materials for supercapacitors, Green. Chem. 19 (2017) 4132–4140.

[44] D. Gandla, X. Wu, F. Zhang, C. Wu, D.Q. Tan, High-performance and high-voltage supercapacitors based on N-doped mesoporous activated carbon derived from dragon fruit peels, ACS Omega 6 (2021) 7615–7625.

[45] H.-h. Fu, L. Chen, H. Gao, X. Yu, J. Hou, G. Wang, F. Yu, H. Li, C. Fan, Y.-l. Shi, et al., Walnut shell-derived hierarchical porous carbon with high performances for electrocatalytic hydrogen evolution and symmetry supercapacitors, Int. J. Hydrog. Energy 45 (2020) 443–451.

[46] F. Gao, J. Qu, Z. Zhao, Z. Wang, J. Qiu, Nitrogen-doped activated carbon derived from prawn shells for high-performance supercapacitors, Electrochim. Acta 190 (2016) 1134–1141.

[47] M. Stefan, C. Leostean, O. Pana, A. Popa, D. Toloman, S. Macavei, I. Perhaita, L. Barbu-Tudoran, D. Silipas, Interface tailoring of SnO₂–TiO₂ photocatalysts modified with anionic/cationic surfactants, J. Mater. Sci. 55 (2020) 3279–3298.

[48] B. Pal, S. Yang, V. Thangadurai, R. Jose, Electrolyte selection for supercapacitive devices: a critical review, Nanoscale Adv. 1 (2019) 3807–3835.

[49] K. Dericiler, A. Kocanali, M. Buldu-Akturk, E. Erdem, B. Saner Okan, Upcycling process of transforming waste coffee into spherical graphene by flash pyrolysis for sustainable supercapacitor manufacturing with virgin graphene electrodes and its comparative life cycle assessment, Biomass Convers. Biorefin. (2022) 1–16.

[50] G.-T. Yu, T.-H. Hsieh, Y.-H. Lin, J.-H. Lin, Porous carbon nanosheets derived from spent coffee grounds for highly stable electric double-layer capacitors enabled by structurally complementary carbons, ACS Sustain. Resour. Manag. 1 (2023) 76–87.

[51] S.V. Sklepova, N. Ivanichok, P. Kolkovskyi, V. Kotsyubynsky, V. Boychuk, B. Rachiy, A. Uhryński, M. Bembenek, L. Ropyak, Porous structure and fractal dimensions of activated carbon prepared from waste coffee grounds, Materials 16 (2023) 6127.

[52] F. Luna-Lama, D. Rodríguez-Padrón, A.R. Puente-Santiago, M.J. Muñoz-Batista, A. Caballero, A.M. Balu, A.A. Romero, R. Luque, Non-porous carbonaceous materials derived from coffee waste grounds as highly sustainable anodes for lithium-ion batteries, J. Clean. Prod. 207 (2019) 411–417.

[53] J.L. GómezUrbano, M.D.L.Á. Moreno Fernández, M. Arnaiz, J. AjuriaArregui, T. RojoAparicio, D. Carriazo, Graphene-coffee waste derived carbon composites as electrodes for optimized lithium ion capacitors author links open overlay panel, Carbon 162 (2020) 273–282.

[54] M.D. Angelin, S. Rajkumar, J.P. Merlin, A.R. Xavier, M. Franklin, A. Ravichandran, Electrochemical investigation of Zr-doped ZnO nanostructured electrode material for high-performance supercapacitor, Ionics 26 (2020) 5757–5772.

[55] T.A. Kandiel, L. Robben, A. Alkaima, D. Bahnemann, Brookite versus anatase TiO₂ photocatalysts: phase transformations and photocatalytic activities, Photochem. Photobiol. Sci. 12 (2013) 602–609.

[56] K. Sathish Kumar, K. Rohit Narayanan, S. Siddarth, R. Pavan Kumar, R. Badri Narayan, R. Goutham, V. Samynaathan, Synthesis of MgO/TiO$_2$ nanocomposite and its application in photocatalytic dye degradation, Int. J. Chem. React. Eng. 16 (2018) 20170136.

[57] Y. Nakagoshi, Y. Suzuki, Pseudobrookite-type MgTi$_2$O$_5$ water purification filter with controlled particle morphology, J. Asian Ceram. Soc. 3 (2015) 334–338.

[58] T. Selvamani, S. Anandan, A.M. Asiri, P. Maruthamuthu, M. Ashok kumar, Preparation of MgTi$_2$O$_5$ nanoparticles for sonophotocatalytic degradation of tri-phenylmethane dyes, Ultrason. Sonochem. 75 (2021) 105585.

[59] H. Zhang, J.F. Banfield, Understanding polymorphic phase transformation behavior during growth of nanocrystalline aggregates: insights from TiO$_2$, J. Phys. Chem. B 104 (2000) 3481–3487.

[60] T. Ohsaka, F. Izumi, Y. Fujiki, Raman spectrum of anatase, TiO$_2$, J. Raman Spectrosc. 7 (1978) 321–324.

[61] M.H. Aleinawi, E. Saritas, M. Stefan, A.U. Ammar, A. Hroub, F.B. Misirlioglu, A. Bocirnea, S. Macavei, S. Tripon, E. Erdem, et al., Supercapacitor devices based on multiphase MgTiO$_3$ perovskites doped with Mn^{2+} ions, Mater. Chem. Phys. 329 (2025) 130016.

[62] A.U. Ammar, A. Popa, D. Toloman, S. Macavei, A. Ciorita, A.-E. Bocirnea, M. Stan, E. Erdem, A.M. Rostas, Nitrogen-doped WO$_3$ nanoparticles as electrode materials in all-in-one supercapacitor devices, ACS Appl. Eng. Mater. 2 (2024) 126–135.

[63] Y. Peter, M. Cardona, Fundamentals of Semiconductors: Physics and Materials Properties, Springer Science & Business Media, Heidelberg, 2010.

[64] J.E. Spanier, R.D. Robinson, F. Zhang, S.-W. Chan, I.P. Herman, Size-dependent properties of CeO$_{2-y}$ nanoparticles as studied by raman scattering, Phys. Rev. B 64 (2001) 245407.

[65] K. Mcguire, Z. Pan, Z. Wang, D. Milkie, J. Menendez, A. Rao, Raman studies of semiconducting oxide nanobelts, J. Nanosci. Nanotechnol. 2 (2002) 499–502.

[66] R. Mahadevaiah, H.S. Lalithamba, S. Shekarappa, R. Hanumanaika, Synthesis of Nα-protected formamides from amino acids using MgO nano catalyst: study of mole-cular docking and antibacterial activity, Sci. Iran. 24 (2017) 3002–3013.

[67] D.K. Pallotti, L. Passoni, P. Maddalena, F. DiFonzo, S. Lettieri, Photoluminescence mechanisms in anatase and rutile TiO$_2$, J. Phys. Chem. C 121 (2017) 9011–9021.

[68] H. Kaftelen, K. Ocakoglu, R. Thomann, S. Tu, S. Weber, E. Erdem, EPR and pho-toluminescence spectroscopy studies on the defect structure of ZnO nanocrystals, Phys. Rev. B—Condens. Matter Mater. Phys. 86 (2012) 014113.

[69] D. Toloman, A. Gungor, A. Popa, M. Stefan, S. Macavei, L. Barbu-Tudoran, A. Varadi, I.D. Yildirim, R. Suciu, I. Nesterovschi, et al., Morphological impact on the supercapacitive performance of nanostructured zno electrodes, Ceramics International (2024).

[70] M. Stefan, A.M. Rostas, A.U. Ammar, A. Gungor, E. Saritas, D. Toloman, A. Varadi, S. Macavei, L. Barbu-Tudoran, C. Leostean, et al., Cerium enhanced supercapacitive properties of zinc oxide nanoflowers, Energy Fuels 38 (2024) 19088–19099.

[71] B. Obeid, A. Hameed, H. Alaaraji, Structural and optical properties of TiO$_2$/MgO thin films preparing at 373 k, Dig. J. Nanomater. Biostruct. 12 (2017) 1239–1246.

[72] P. Basyach, A. Choudhury, Structural and optical properties of core-shell TiO$_2$/MgO nanostructures at different annealing temperatures, Int. J. Innov. Res. Dev. 1 (2012) 175–180.

[73] L. Borkovska, L. Khomenkova, I. Markevich, M. Osipyonok, T. Stara, O. Gudymenko, V. Kladko, M. Baran, S. Lavoryk, X. Portier, et al., Effect of Li$^+$ co-doping on structural and luminescence properties of Mn^{4+} activated magnesium titanate films, J. Mater. Sci.: Mater. Electron. 29 (2018) 15613–15620.

[74] D.M. Murphy, R.D. Farley, I.J. Purnell, C.C. Rowlands, A.R. Yacob, M.C. Paganini, E. Giamello, Surface defect sites formed on partially and fully dehydrated MgO: an EPR/ENDOR study, J. Phys. Chem. B 103 (1999) 1944–1953.

[75] A. Naldoni, M. Altomare, G. Zoppellaro, N. Liu, S. Kment, R. Zboril, P. Schmuki, Photocatalysis with reduced TiO$_2$: from black TiO$_2$ to cocatalyst-free hydrogen production, ACS Catal. 9 (2018) 345–364.

[76] S. Stoll, A. Schweiger, Easyspin, a comprehensive software package for spectral simulation and analysis in EPR, J. Magn. Reson. 178 (2006) 42–55.

[77] W. Low, Paramagnetic resonance spectrum of manganese in cubic MgO and CaF$_2$, Phys. Rev. 105 (1957) 793.

[78] D. Dvoranová, V. Brezová, M. Mazúr, M.A. Malati, Investigations of metal-doped titanium dioxide photocatalysts, Appl. Catal. B: Environ. 37 (2002) 91–105.

[79] J. Han, P. Mantas, A. Senos, Defect chemistry and electrical characteristics of un-doped and Mn-doped ZnO, J. Eur. Ceram. Soc. 22 (2002) 49–59.

[80] B.-A. Mei, O. Munteshari, J. Lau, B. Dunn, L. Pilon, Physical interpretations of nyquist plots for EDLC electrodes and devices, J. Phys. Chem. C 122 (2018) 194–206.

[81] S. Wang, J. Zhang, O. Gharbi, V. Vivier, M. Gao, M.E. Orazem, Electrochemical impedance spectroscopy, Nat. Rev. Methods Prim. 1 (2021) 41.

[82] R.K. Mishra, G.J. Choi, H.J. Choi, J. Singh, F.S. Mirsafi, H.-G. Rubahn, Y.K. Mishra, S.H. Lee, J.S. Gwag, Voltage holding and self-discharge phenomenon in ZnO–Co$_3$O$_4$ core-shell heterostructure for binder-free symmetric supercapacitors, Chem. Eng. J. 427 (2022) 131895.

[83] M.Z.U. Shah, M.S. Javed, M. Sajjad, A. Shah, M.S. Shah, S. UrRahman, A. Mahmood, M. Ahmad, M.A. Assiri, H. Hou, A novel TiO$_2$/CuSe based nano-composite for high-voltage asymmetric supercapacitors, J. Sci.: Adv. Mater. Devices 7 (2022) 100418.

[84] K. Karthikeyan, S. Amaresh, V. Aravindan, Y. Lee, Microwave assisted green synthesis of MgO–carbon nanotube composites as electrode material for high power and energy density supercapacitors, J. Mater. Chem. A 1 (2013) 4105–4111.

[85] G. Zamiri, A.M.A. Haseeb, P. Jagadish, M. Khalid, I. Kong, S.G. Krishnan, Three-dimensional graphene-TiO$_2$–SnO$_2$ ternary nanocomposites for high-performance asymmetric supercapacitors, ACS Omega 7 (2022) 43981–43991.

[86] W. Zhong, H. Sun, J. Pan, Y. Zhang, X. Yan, Y. Guan, W. Shen, X. Cheng, Hierarchical porous TiO$_2$/carbide-derived carbon for asymmetric supercapacitor with enhanced electrochemical performance, Mater. Sci. Semicond. Process. 127 (2021) 105715.

[87] Y.-G. Wang, Z.-D. Wang, Y.-Y. Xia, An asymmetric supercapacitor using RuO$_2$/TiO$_2$ nanotube composite and activated carbon electrodes, Electrochim. Acta 50 (2005) 5641–5646.

[88] S.-Y. Hsu, F.-H. Hsu, J.-L. Chen, Y.-S. Cheng, J.-M. Chen, K.-T. Lu, The super-capacitor electrode properties and energy storage mechanism of binary transition metal sulfide MnCo$_2$S$_4$ compared with oxide MnCo$_2$O$_4$ studied using in situ quick X-ray absorption spectroscopy, Mater. Chem. Front. 5 (2021) 4937–4949.

[89] H. Wang, N. Mi, S. Sun, W. Zhang, S. Yao, Oxygen vacancies enhancing capacitance of MgCo$_2$O$_4$ for high performance asymmetric supercapacitors, J. Alloy. Compd. 869 (2021) 159294.

[90] W. Naffouti, A. Jrad, T. BenNasr, S. Ammar, N. Turki-Kamoun, Structural, mor-phological and optical properties of TiO$_2$: Mn thin films prepared by spray pyrolysis technique, J. Mater. Sci.: Mater. Electron. 27 (2016) 4622–4630.

[91] C. Lin, D. Channei, P. Koshy, A. Nakaruk, C. Sorrell, Multivalent Mn-doped TiO$_2$ thin films, Phys. E: Low. -Dimens. Syst. Nanostruct. 44 (2012) 1969–1972.

[92] A. Elmouwahidi, E. Bailón-García, A. Castelo-Quibén, A. Pérez-Cadenas, F. Maldonado-Hódar, F. Carrasco-Marín, Carbon–TiO$_2$ composites as high-performance supercapacitor electrodes: synergistic effect between carbon and metal oxide phases, J. Mater. Chem. A 6 (2018) 633–644.